Computational model of a Calcium-looping fluidized bed calcination reactor with imposed concentrated solar irradiance

D. Rodrigues [a,b,c,*], M. Alvarez Rivero [c], C.I.C. Pinheiro [a,c], J.P. Cardoso [d], L.F. Mendes [e,f]

[a] Centro de Química Estrutural, Institute of Molecular Sciences, Instituto Superior Técnico, Universidade de Lisboa, Av. Rovisco Pais 1, 1049-001 Lisboa, Portugal
[b] Centro de Recursos Naturais e Ambiente, Instituto Superior Técnico, Universidade de Lisboa, Av. Rovisco Pais 1, 1049-001 Lisboa, Portugal
[c] Departamento de Engenharia Química, Instituto Superior Técnico, Universidade de Lisboa, Av. Rovisco Pais 1, 1049-001 Lisboa, Portugal
[d] Laboratório Nacional de Energia e Geologia, I.P., Estrada do Paço do Lumiar 22, 1649-038 Lisboa, Portugal
[e] IN+/LARSyS, Instituto Superior Técnico, Universidade de Lisboa, Av. Rovisco Pais 1, 1049-001 Lisboa, Portugal
[f] Departamento de Física, Instituto Superior Técnico, Universidade de Lisboa, Av. Rovisco Pais 1, 1049-001 Lisboa, Portugal

ARTICLE INFO

ABSTRACT

The Calcium-looping process is a promising option for thermochemical energy storage in concentrating solar power plants. A crucial element of this process is the solar calcination reactor, where the endothermic reaction of $CaCO_3$ calcination occurs with formation of CaO and CO_2. The solar energy that is chemically stored in the reaction products can be retrieved by the exothermic reaction of CaO carbonation when needed. In this article, a new computational model is developed for the solar calcination reactor in this Calcium-looping process. The calcination reaction takes place in the riser of a continuous circulating fluidized bed that corresponds to an absorber tube exposed to concentrated solar radiation, which allows the reaction chamber to be indirectly heated. A core-annulus heat transfer model and a modified version of the Kunii–Levenspiel fluid dynamics model are used. In contrast to previous models found in the literature, the change in the mass flow rate of the species and in the density of the phases due to the reaction is considered. Simulation studies are performed with a fixed and imposed concentrated solar irradiance on the reactor wall, which varies in both the axial and angular directions. Wall conduction in the angular direction is also considered. The results show that nearly complete calcination can be achieved with a reactor of 4 m of height. A sensitivity analysis with respect to the model parameters and inlet conditions shows that the calcination conversion is mostly affected by the solids mass flow rate and the bed temperature at the inlet.

1. Introduction

Concentrating solar power (CSP) systems rely on the concentration of solar energy into a small receiver area. Concentrated solar energy (CSE) coupled with thermal energy storage (TES) has been proposed as a useful and cost-effective way to address the inherent variability of renewable energy sources such as solar and wind, owing to the high temperatures that it can achieve (Schöniger et al., 2021). The most commonly used solution for TES relies on nitrate-based molten salts, which leads to several disadvantages. More specifically, this solution does not allow surpassing a value around 600 °C for the working temperature, which poses limits on the system efficiency, and it requires energy consumption to avoid solidification (Vignarooban et al., 2015). On the other hand, thermochemical energy storage (TCES) allows storing solar energy by means of a reversible reaction involving carbonates, hydroxides, oxides, or hydrides, for example. Solar energy is used to carry out an endothermic reaction and the chemically stored energy is retrieved by carrying out the reverse exothermic reaction when needed (Lovegrove and Stein, 2012).

One of the systems for TCES is the Calcium-looping (CaL) process, which corresponds to a cycle that comprises: (i) an endothermic reaction that consists in the calcination of $CaCO_3$ with generation of CaO and CO_2; (ii) an exothermic reaction where $CaCO_3$ is formed via carbonation of CaO in the presence of CO_2. The CaL process is considered a promising option with respect to other TCES methods owing to the large energy density (mostly in the chemical form), the low cost, abundance, and harmlessness of natural $CaCO_3$ sources such as limestone, or even the beneficial use of waste materials such as waste marble powder suggested by Pinheiro et al. (2016) and Teixeira et al. (2022), with respect to both the environment and human health, and

Nomenclature

Abbreviations

CaL	Calcium looping
CFB	Circulating fluidized bed
CSE	Concentrated solar energy
CSP	Concentrating solar power
HTC	Heat transfer coefficient
TCES	Thermochemical energy storage
TES	Thermal energy storage
TRL	Technology readiness level

Latin symbols

A	Cross-section area [m^2]
a	Decay factor [m^{-1}]
a_0	Proportionality constant for a [s^{-1}]
Ar	Archimedes number [–]
$c_{CO_2}/c_{CO_2,eq}$	Local/equilibrium concentration of CO_2 in the gas [mol m^{-3}]
$C_{P,c}$	Cluster specific heat capacity [J kg^{-1} K^{-1}]
$C_{P,g}/C_{P,s}$	Specific heat capacity of the gas/solids [J kg^{-1} K^{-1}]
$C_{P,i}$	Temperature-dependent specific heat capacity of species i [J kg^{-1} K^{-1}]
c_s	Number of moles of solids per unit of reactor volume [mol m^{-3}]
D	Reactor diameter [m]
d_p	Particle diameter [m]
d_w	Wall thickness [m]
e_c/e_d	Emissivity of the clusters/disperse phase [–]
e'_p	Effective emissivity of a particle cloud [–]
e_s/e_w	Emissivity of the particle surface/wall [–]
g	Gravity acceleration [m s^{-2}]
$h_{c,i}/h_{d,i}$	HTC from the clusters/disperse phase to the ith element [W m^{-2} K^{-1}]
$h_{c,rad}/h_{d,rad,i}$	HTC of radiation from the clusters/disperse phase to the ith element [W m^{-2} K^{-1}]
$\widetilde{H}_{calc}$	Power per unit of length for the reaction kinetics [W m^{-1}]
H_{dense}	Height of the dense bed [m]
$H_{e-w,i}/H_{w-b,i}$	Environment-wall/wall-bed heat flux at the ith element [W m^{-2}]
$\widetilde{H}_{g-s}/\widetilde{H}_{w-b}$	Power per unit of length for the gas–solid/wall-bed heat transfer [W m^{-1}]
$\widetilde{h}_{g-s}/\widetilde{h}_{w-b}$	Gas–solid/total wall-bed HTC per unit of length [W m^{-1} K^{-1}]
$H_{irr,i}$	Concentrated solar irradiance on the ith element [W m^{-2}]
$h_{r,rad,i}$	HTC of radiation from the receiver cavity to the ith element [W m^{-2} K^{-1}]
H_t	Total reactor height [m]
$h_{w-b,i}$	Total wall-bed HTC in the ith element [W m^{-2} K^{-1}]
k_c/k_w	Cluster/wall thermal conductivity [W m^{-1} K^{-1}]
k_{calc}	Kinetic constant of $CaCO_3$ calcination reaction [m^3 mol^{-1} s^{-1}]
k_g/k_s	Gas/solids thermal conductivity [W m^{-1} K^{-1}]

$k_{gf,i}$	Gas thermal conductivity evaluated at $T_{f,i}$ [W m^{-1} K^{-1}]
$\dot{m}_g/\dot{m}_s$	Total mass flow rate of gas/solids [kg s^{-1}]
M_i	Molar mass of species i [kg mol^{-1}]
$\dot{m}_i$	Mass flow rate of species i [kg s^{-1}]
n_{el}	Number of elements of the wall in the simulation [–]
Nu	Nusselt number [–]
Pr	Prandtl number [–]
R	Ideal gas constant [J mol^{-1} K^{-1}]
r_{calc}	Reaction rate of $CaCO_3$ calcination [mol m^{-3} s^{-1}]
Re	Reynolds number [–]
R_i	Specific ideal gas constant of the gas species i [J kg^{-1} K^{-1}]
T_b/T_{ref}	Bed/reference temperature [K]
t_c	Average residence time of clusters on the wall [s]
$T_{c,i}/T_{f,i}$	Cluster/mean gas-film temperature at the ith element [K]
T_g/T_s	Gas/solids temperature [K]
T_r	Temperature of the receiver cavity [K]
t_s	Solids residence time [s]
$\bar{T}_w$	Maximum mean wall temperature [K]
$T_{w,i}$	Wall temperature in the ith element [K]
U_0	Superficial gas velocity [m s^{-1}]
U_g/U_s	Gas/solids velocity [m s^{-1}]
U_t	Terminal velocity of particles [m s^{-1}]
w_{CaO}/w_{CO_2}	Mass fraction of CaO in the solid phase/CO_2 in the gas phase [–]
X_i	Molar fraction of species i in its phase [–]
z	Axial position on the reactor [m]

Greek symbols

α	Volumetric gas–solid HTC [W m^{-3} K^{-1}]
α_p	Gas-particle HTC [W m^{-2} K^{-1}]
δ_c	Fraction of the wall in contact with clusters [–]
$\Delta H_{calc}(T_b)$	Enthalpy of $CaCO_3$ calcination reaction at T_b [J mol^{-1}]
ΔH^0_{calc}	Standard enthalpy of $CaCO_3$ calcination reaction at T_{ref} [J mol^{-1}]
$\varepsilon_c/\varepsilon_{cw}$	Gas volumetric fraction within the clusters/near the wall [–]
$\varepsilon_g/\varepsilon_s$	Gas/solids volumetric fraction [–]
$\varepsilon_{s,d}$	Solids volumetric fraction of the disperse phase near the wall [–]
ε'_s	Solids volumetric fraction in choked condition [–]
η_{calc}	Molar calcination conversion [–]
μ_g	Gas viscosity [kg m^{-1} s^{-1}]
ν_i	Stoichiometric coefficient of species i in $CaCO_3$ calcination [–]
ρ_c/ρ_d	Density of the clusters/disperse phase [kg m^{-3}]
ρ_g/ρ_s	Local density of the gas/solids [kg m^{-3}]
ρ_i	Density of species i [kg m^{-3}]
ρ_{susp}	Average suspension density [kg m^{-3}]
σ	Stefan–Boltzmann constant [W m^{-2} K^{-4}]

Calligraphic symbols	
$\mathcal{S}_f$	Set of species in the phase f
Subscripts	
b	Fluidized bed
c	Clusters
$calc$	$CaCO_3$ calcination reaction
d	Disperse phase
$dense$	Dense zone
f	Generic phase
g	Gas phase
$lean$	Lean zone
p	Particle
r	Receiver cavity
rad	Radiation
s	Solid phase
w	Reactor wall
Superscripts	
$*$	Saturation carrying capacity condition

the high temperature of the exothermic carbonation reaction, which allows higher thermal-to-electrical efficiencies than molten salts. In the CaL process for TCES, the endothermic calcination of $CaCO_3$ is carried out in a solar reactor using concentrated solar radiation as energy source (Pardo et al., 2014; Ortiz et al., 2019).

The CaL process for post-combustion CO_2 capture has been thoroughly studied in the literature and demonstrated in laboratory-scale and pilot plant experimental studies (Charitos et al., 2011; Arias et al., 2013, 2018). In many of these studies, continuous circulating fluidized bed (CFB) reactors have been used for both the calcination and the carbonation reactions owing to their high mass and heat transfer rates, effective solids mixing, and adjustable residence time (Hanak et al., 2015; Martínez et al., 2016). However, in that process, calcination is typically combined with oxy-fuel combustion at high CO_2 concentrations and temperatures to supply the required energy (Arias et al., 2018). In contrast, the calcination reaction in the CaL process for TCES requires the supply of solar energy, but it can be performed at lower CO_2 concentrations and temperatures. Note that the CaL process for TCES does not lead to net CO_2 emissions since it also includes a carbonation reaction where the CO_2 reacts with CaO to regenerate $CaCO_3$. However, the development of the CaL process for TCES is still at an initial stage, with a technology readiness level (TRL) of 4–5 (Ortiz et al., 2019).

Hence, although solar reactors for $CaCO_3$ calcination are a crucial element of the CaL process for TCES, to the best of our knowledge no models have been developed for simulation of these reactors which encompass the effects of fluid dynamics, reaction kinetics, and heat transfer, including the interaction with concentrated solar radiation. A first step was given in this direction by Lisbona et al. (2020), who proposed a model for a solar entrained flow calcination reactor in a CSP plant by dividing the reactor wall in stages with constant heat flux. However, the fluid dynamics and heat transfer models in that work are rather simple since they do not consider the existence of several zones in the reactor and the effect of concentrated solar irradiance, for example. Several models of calcination reactors for the CaL process for post-combustion CO_2 capture have been developed. Ylätalo et al. (2013) modeled the oxy-combustion calcination reactor in the post-combustion CaL process at steady state and concluded that a 1-dimensional model produces similar results to a more detailed 3-dimensional model. Martínez et al. (2013) proposed a calcination

reactor model based on simple fluid-dynamic assumptions and calcination kinetics and obtained operating windows where high calcination efficiencies are achieved. Sánchez and Jakobsen (2014) proposed a model of two coupled CFBs for a calcination/carbonation loop, where each gas–solid reactor was described by a dynamic one-dimensional two-fluid model based on fluid dynamics. Cormos and Simon (2015) also developed one-dimensional dynamic models of two CFBs for calcination and carbonation in the fast fluidization regime, which allowed obtaining time-varying profiles for the solids and gas flows and the temperature.

In this paper, the current gap in the literature is addressed by developing a novel mathematical model of a continuous CFB reactor for solar calcination of $CaCO_3$ and demonstrating it via simulation studies. This model includes mass balances, fluid dynamics, and energy balance. The mass and energy balances account for reaction kinetics, enthalpy of reaction, and heat transfer. The model considers changes in the mass flow rate and density resulting from the reaction, similarly to our previous work (Rivero et al., 2021). The novelty with respect to this previous work is the fact that the present model considers imposed concentrated solar irradiance on the reactor wall, variations of wall temperature and wall-bed heat transfer flux in both the axial and angular directions, and wall conduction in the angular direction. The simulation studies also include a sensitivity analysis with respect to several model parameters and inlet conditions to identify how they affect the reactor conversion and other key variables.

Ideally, this model should be validated via comparison with experimental results in the literature. Some examples of solar-driven reactors for calcination of $CaCO_3$ were presented in the literature, mostly in a directly irradiated configuration, including rotary reactors (Meier et al., 2004), entrained bed reactors (Nikulshina et al., 2006), and fluidized bed reactors (Nikulshina et al., 2009). However, to the best of our knowledge, and in agreement with our review paper (Alvarez Rivero et al., 2022), no detailed experimental results are available in the literature concerning fluidized bed reactors where calcination of $CaCO_3$ takes place and the heat for the calcination reaction is supplied by solar radiation on the reactor wall. A possible cause for this gap in the literature is the fact that, as mentioned, the most developed CaL process is the one for post-combustion CO_2 capture with oxy-combustion in the calcination reactor, where external heat sources such as solar energy have not been used for calcination of $CaCO_3$. In contrast, the CaL process for TCES is less developed, which justifies the lack of experimental results in this context.

This paper is organized as follows. Section 2 presents the mathematical model, in particular the mass and energy balance equations and the fluid dynamics model, the performance indicators, and the model parameters and boundary conditions used for simulation. Section 3 shows and discusses the simulation results for the reference conditions and the sensitivity analysis with respect to the selected variables, and Section 4 concludes the paper.

2. Mathematical model

2.1. Overview

Calcination of $CaCO_3$ is an endothermic reaction that regenerates CaO and releases CO_2. The calcination reaction is described by the equation

$$CaCO_3\,(s) \Leftrightarrow CaO\,(s) + CO_2\,(g), \tag{1}$$

where $\Delta H^0_{calc} = 178.4 \times 10^3$ J mol^{-1} is the standard enthalpy of $CaCO_3$ calcination reaction at the reference temperature $T_{ref} = 298.15$ K and 1 atm. The reactor to be modeled contains the solid species $CaCO_3$ and CaO and the gas species water and CO_2, where the water is used as fluidizing gas to reduce the CO_2 concentration, which promotes the calcination reaction.

In this paper, a reactor configuration that consists in a cylindrical absorber tube is proposed, allowing the reaction chamber to be indirectly heated by exposing the walls to concentrated solar radiation. This tube plays the role of a riser of a continuous CFB. Both the gas phase and the solid phase are introduced at the bottom of the reactor. The operating conditions for the CFB reactor are selected based on existing lab-scale and pilot-scale calcination reactors for the CaL process. Typically, these reactors are designed for low solids fluxes, below 30 kg m^{-2} s^{-1}, and superficial gas velocities in a range of 1.5–6 m s^{-1} (Charitos et al., 2011; Arias et al., 2013), which corresponds to the low-density CFB region (Sun and Zhu, 2019). Hence, a fast fluidization regime is considered for this reactor model. The fast fluidization regime occurs when two conditions are satisfied: the gas velocity is beyond the transport velocity, when a sharp increase of the particle carryover occurs; the gas velocity is not sufficient to achieve a pneumatic transport regime, which leads to a very dilute suspension flow where both the axial and radial distributions of the solids holdup are uniform (Sun and Zhu, 2019). It is empirically observed that two regions can be found in a fast fluidized bed: the dense zone, which is located in the lower part of the riser, where the solids volumetric fraction is almost constant and in the order of 0.15–0.22, followed by the lean zone, where the solids are entrained, and a progressive decrease of their volumetric fraction takes place. A core-annulus pattern describes the flow in the lean zone. In this zone, the cross-section is divided into two regions: a homogeneous core with disperse solid particles fluidized by the gas moving upwards, and a smaller annulus region where the solids are denser. In the annulus region, clusters flow down over the wall for a certain distance, detach themselves from the wall, and are re-entrained and mixed with fresh particles in the core region (Kunii and Levenspiel, 1991).

2.2. Model assumptions

The proposed mathematical model relies on several assumptions, as follows: (a) the diffusivity terms (for mass diffusion and heat conduction within the flow) are neglected; (b) the reactor is at steady state; (c) the static pressure due to the particles is neglected; (d) the gas species are ideal gases; (e) in the dense zone and in each mesh element of the lean zone in the axial direction of the reactor, the thermophysical properties of the species are constant; (f) the solids volumetric fraction in the dense zone is calculated with an experimental correlation, and the solids volumetric fraction in the lean zone is described by an adaptation of the K-L model (Kunii and Levenspiel, 1991); (g) in each mesh element in the axial direction of the reactor, the velocity of all the gas species is the same, and the velocity of all the solid species is the same, but the velocity of the gas species may be different from the velocity of the solid species; (h) the solid particles are considered to be spheres with a single radius; (i) the heat transfer in the lean zone is described by a core-annulus model; (j) the heat transfer between the reactor wall and the fluidized bed is modeled with a total heat transfer coefficient (HTC) for each mesh element of the wall; (k) the solids and the gas are in thermal equilibrium in each mesh element; (l) the energy of the flow is due to its enthalpy only (variations of kinetic and potential energy are neglected); (m) the reactor is enclosed by a cavity at a constant temperature; (n) heat loss due to convection from the reactor to its surroundings is neglected. In this work, in contrast to previous work (Rivero et al., 2021), the elements in (j) are discretized not only in the axial direction but also in the angular direction, and wall conduction in the angular direction is considered. The model is expected to be equally valid for any reactor dimensions, ranging from lab scale to industrial scale.
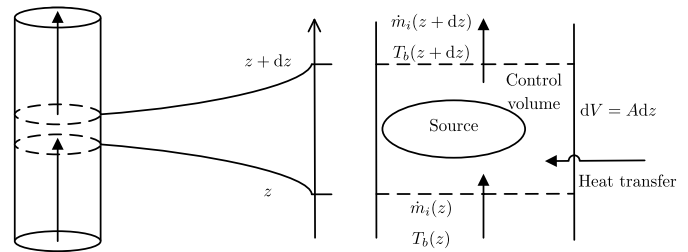

Fig. 1. Schematic of a control volume (on the right) of the reactor (on the left) used for the mass and heat balances.

2.3. Mass balance equations

From a mass balance in a control volume of the reactor for steady-state conditions such as the one shown in Fig. 1, the mass balance for each solid species as a function of the axial position on the reactor z (m) is:

$$\frac{d\dot{m}_i(z)}{dz} = \nu_i M_i r_{calc}(z) A, \qquad i \in \{CaCO_3, CaO\}, \tag{2}$$

with the reaction rate r_{calc} of $CaCO_3$ calcination (mol m^{-3} s^{-1})

$$r_{calc}(z) = c_s(z) k_{calc}(z) X_{CaCO_3}(z)^{2/3} \left(c_{CO_2,eq}(z) - c_{CO_2}(z) \right), \tag{3}$$

and the boundary conditions

$$\dot{m}_{CaCO_3}(0) = \left(1 - w_{CaO}(0) \right) \dot{m}_s(0), \tag{4}$$

$$\dot{m}_{CaO}(0) = w_{CaO}(0) \dot{m}_s(0), \tag{5}$$

where $\dot{m}_i$ is the mass flow rate of species i (kg s^{-1}), ν_i is the stoichiometric coefficient in $CaCO_3$ calcination (-), M_i is the molar mass (kg mol^{-1}), X_i is the molar fraction in its phase (-), c_s is the number of moles of solids per unit of reactor volume (mol m^{-3}), c_{CO_2} is the local concentration of CO_2 (mol m^{-3}), A is the cross-section area (m^2), $w_{CaO}(0)$ is the inlet mass fraction of CaO in the solid phase (-), and $\dot{m}_s(0)$ is the inlet mass flow rate of solids (kg s^{-1}). As proposed by Martínez et al. (2013) and Fang et al. (2009), the kinetic constant k_{calc} of $CaCO_3$ calcination reaction (m^3 mol^{-1} s^{-1}) and the equilibrium concentration $c_{CO_2,eq}$ of CO_2 in the gas (mol m^{-3}) are:

$$k_{calc}(z) = 2.05 \times 10^3 e^{-\frac{1.12 \times 10^5}{RT_s(z)}}, \tag{6}$$

$$c_{CO_2,eq}(z) = \frac{1.462 \times 10^{11}}{T_g(z)} e^{-\frac{1.913 \times 10^4}{T_g(z)}}, \tag{7}$$

where $R = 8.314$ J mol^{-1} K^{-1} is the ideal gas constant, T_s is the solids temperature (K) and T_g is the gas temperature (K). The term on the right-hand side of (2) corresponds to the source term in Fig. 1.

By mass conservation, the mass flow rates of CO_2 and of water used as fluidizing gas (kg s^{-1}) are given by

$$\dot{m}_{CO_2}(z) = \dot{m}_{CO_2}(0) + \dot{m}_s(0) - \dot{m}_s(z), \tag{8}$$

$$\dot{m}_{H_2O}(z) = \dot{m}_{H_2O}(0), \tag{9}$$

with the boundary conditions

$$\dot{m}_{CO_2}(0) = w_{CO_2}(0) \dot{m}_g(0), \tag{10}$$

$$\dot{m}_{H_2O}(0) = \left(1 - w_{CO_2}(0) \right) \dot{m}_g(0), \tag{11}$$

where $w_{CO_2}(0)$ is the inlet mass fraction of CO_2 in the gas phase (-) and $\dot{m}_g(0)$ is the inlet mass flow rate of gas (kg s^{-1}).

The total mass flow rate $\dot{m}_f$ of the generic phase f (kg s^{-1}) can be obtained from

$$\dot{m}_f(z) = \sum_{i \in S_f} \dot{m}_i(z), \qquad f \in \{s, g\}, \tag{12}$$

where s denotes the solid phase, g denotes the gas phase, and S_f denotes the set of species in the phase f.

The molar fractions of the species in the phase f are

$$X_i(z) = \frac{\frac{\dot{m}_i(z)}{M_i}}{\sum_{j \in S_f} \frac{\dot{m}_j(z)}{M_j}}, \qquad i \in S_f. \tag{13}$$

The local densities $\rho_s(z)$ of the solids and $\rho_g(z)$ of the gas (kg m^{-3}) can be calculated as

$$\rho_s(z) = \frac{\rho_{CaO}\rho_{CaCO_3}}{(1-w_{CaO}(z))\rho_{CaO}+w_{CaO}(z)\rho_{CaCO_3}}, \tag{14}$$

$$\rho_g(z) = \frac{\rho_{CO_2}(z)\rho_{H_2O}(z)}{\left(1-w_{CO_2}(z)\right)\rho_{CO_2}(z)+w_{CO_2}(z)\rho_{H_2O}(z)}, \tag{15}$$

where the mass fractions w_{CaO} of CaO or w_{CO_2} of CO_2 in the corresponding phase $p_{CaO} = s$ or $p_{CO_2} = g$ (-) are

$$w_i(z) = \frac{\dot{m}_i(z)}{\dot{m}_{p_i}(z)}, \qquad i \in \{CaO, CO_2\}, \tag{16}$$

and the density ρ_i of the gas species i (kg m^{-3}) is a function of the specific ideal gas constant R_i (J kg^{-1} K^{-1}) given by

$$\rho_i(z) = \frac{P}{R_i T_g(z)}, \qquad i \in \{CO_2, H_2O\}. \tag{17}$$

The solids concentration and the local concentration of CO_2 are described by:

$$c_s(z) = \frac{1}{U_s(z)A}\left(\frac{\dot{m}_{CaO}(z)}{M_{CaO}} + \frac{\dot{m}_{CaCO_3}(z)}{M_{CaCO_3}}\right), \tag{18}$$

$$c_{CO_2}(z) = \frac{\dot{m}_{CO_2}(z)}{M_{CO_2} U_g(z)A\varepsilon_g(z)}, \tag{19}$$

where U_s and U_g are the solids and gas velocities (m s^{-1}) given by

$$U_s(z) = \frac{1}{\varepsilon_s(z)A}\left(\frac{\dot{m}_{CaO}(z)}{\rho_{CaO}} + \frac{\dot{m}_{CaCO_3}(z)}{\rho_{CaCO_3}}\right), \tag{20}$$

$$U_g(z) = \frac{1}{\varepsilon_g(z)A}\left(\frac{\dot{m}_{CO_2}(z)}{\rho_{CO_2}(z)} + \frac{\dot{m}_{H_2O}(z)}{\rho_{H_2O}(z)}\right), \tag{21}$$

ε_g is the gas volumetric fraction (-) given by

$$\varepsilon_g(z) = 1 - \varepsilon_s(z), \tag{22}$$

and ε_s is the solids volumetric fraction (-), which is computed according the fluid dynamics model below.

2.4. Fluid dynamics model

The K-L model proposed by Kunii and Levenspiel (1991) describes the fluid dynamics in the riser, which is used to compute the solids volumetric fraction ε_s in the dense and lean zones:

$$\varepsilon_s(z) = \begin{cases} \varepsilon_{s,dense} & z \in [0; H_{dense}] \\ \varepsilon_{s,lean}(z) & z > H_{dense} \end{cases}, \tag{23}$$

with

$$\varepsilon_{s,dense} = \begin{cases} 0.2369 U_0(0)^{-0.274} & U_0(0) \in [1.5; 5.0] \text{ m s}^{-1} \\ 0.15 & U_0(0) > 5.0 \text{ m s}^{-1} \end{cases}, \tag{24}$$

$$\varepsilon_{s,lean}(z) = \varepsilon_s^* + \left(\varepsilon_{s,dense} - \varepsilon_s^*\right) e^{-a(z-H_{dense})}, \tag{25}$$

where the subscripts $lean$ and $dense$ denote the lean and dense zones of the riser, ε_s^* is the solids volumetric fraction at saturation carrying capacity condition[1] (-), a is the decay factor (m^{-1}), and H_{dense} is the height of the dense bed (m). The parameter a describes the sigmoidal

---

[1] The saturated carrying capacity condition is reached after an infinite reactor length, when pneumatic transport occurs, that is, when the solids and the gas have the same velocity.
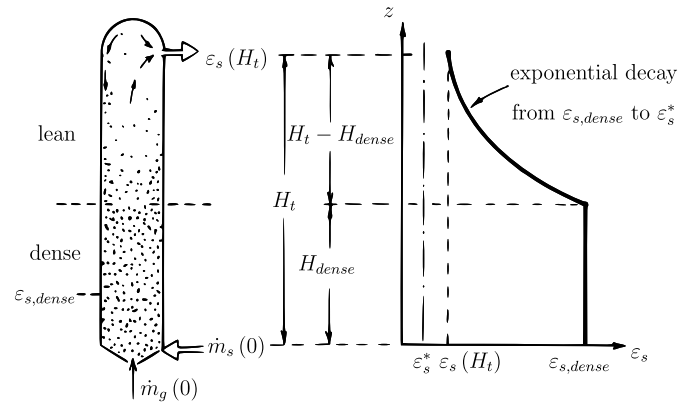

Fig. 2. Variation of the solids volumetric fraction with the reactor height, which gives an insight into the fluid dynamics described by the K-L model.
Source: Adapted from Kunii and Levenspiel (2000).

shape of $\varepsilon_s(z)$ in the lower part of the lean zone and ε_s^* is the asymptotic limit of $\varepsilon_s(z)$. The correlation (24) is used to compute the solids volumetric fraction $\varepsilon_{s,dense}$ in the dense zone based on data from Kunii and Levenspiel (1991). Fig. 2 shows a typical variation of the solids volumetric fraction with the reactor height.

It is assumed in the literature that the decay factor depends on the superficial gas velocity U_0 (m s^{-1}), which is the velocity that the gas would have if it occupied the whole section of the reactor:

$$U_0(z) = \frac{\dot{m}_g(z)}{\rho_g(z)A}. \tag{26}$$

Kunii and Levenspiel (1991) presented experimental values of a for operating conditions that match the ones in this work, although the mass flow rates were constant in the former case. According to those results, a is given by

$$a = \frac{a_0}{U_0(H_{dense})}, \tag{27}$$

with the proportionality constant $a_0 \in [4; 12]$ s^{-1}.

When cold columns with constant solids and gas mass flow rates along the axial direction and without reactions are considered, the changes in velocities are exclusively caused by changes in volumetric fractions. The gas velocity starts at a maximum value and the solids velocity starts at a minimum value. Then, they vary monotonically and converge to the pneumatic transport conditions. However, when the gas mass flow rate and the temperature increase due to the reaction and the heat transfer, respectively, the gas velocity increases as well. Hence, the K-L model must be adapted to deal with these factors.

Since the gas velocity increases, the saturation carrying capacity is smaller than predicted by the K-L model. The solids volumetric fraction ε_s^* at saturated carrying capacity condition, which is the same as the asymptotic value of solids volumetric fraction, is found in this study by assuming that the particles are fully converted in the calcination reaction and that they reach pneumatic transport conditions (i.e. the gas and solids have the same velocity).

In the following equations, the superscript * denotes quantities for the saturated carrying capacity condition. The assumption of pneumatic transport for the saturated carrying capacity leads to the following equation:

$$U_s^* = U_g^* \simeq U_0^*. \tag{28}$$

The mass flow rate of CaO for this condition corresponds to the initial value plus the mass flow rate of CaO that results from the assumption that all the $CaCO_3$ is converted to CaO:

$$\dot{m}_{CaO}^* = \dot{m}_{CaO}(0) + \frac{M_{CaO}}{M_{CaCO_3}}\dot{m}_{CaCO_3}(0). \tag{29}$$

The mass flow rate of gas and CO_2 for this condition are the initial ones plus the mass flow rate of CO_2 released in the complete calcination process:

$$\dot{m}_g^* = \dot{m}_g(0) + \frac{M_{CO_2}}{M_{CaCO_3}}\dot{m}_{CaCO_3}(0), \tag{30}$$

$$\dot{m}_{CO_2}^* = \dot{m}_{CO_2}(0) + \frac{M_{CO_2}}{M_{CaCO_3}}\dot{m}_{CaCO_3}(0). \tag{31}$$

The solids volumetric fraction ε_s^* can then be found by solving (20) as

$$\varepsilon_s^* = \frac{\dot{m}_{CaO}^*}{\rho_{CaO}U_s^*A} \simeq \frac{\dot{m}_{CaO}^*}{\rho_{CaO}U_0^*A}, \tag{32}$$

where the superficial gas velocity U_0^* can be determined by applying (26) to this case, which yields

$$U_0^* = \frac{\dot{m}_g^*}{\rho_g^*A}, \tag{33}$$

and (15), (16), and (17) can be used to compute the gas density ρ_g^* as

$$\rho_g^* = \frac{\rho_{CO_2}^*\rho_{H_2O}^*}{(1-w_{CO_2}^*)\rho_{CO_2}^* + w_{CO_2}^*\rho_{H_2O}^*}, \tag{34}$$

with

$$w_{CO_2}^* = \frac{\dot{m}_{CO_2}^*}{\dot{m}_g^*} \tag{35}$$

and

$$\rho_i^* = \frac{P}{R_iT_g^*}, \qquad i \in \{CO_2, H_2O\}. \tag{36}$$

For high-temperature reactions, as in this case, additional assumptions have to be added regarding the gas temperature T_g^* at saturated carrying capacity condition. By varying this temperature in an interval of 650–1000 °C, it can be verified that the obtained range ε_s^* is narrow and the simulation results are insensitive to ε_s^* in this range. Then, a possible approach to choose this temperature is to assume that it is equal to the gas temperature after an infinite reactor length. Since it is expected that the gas temperature reaches the temperature T_r of the receiver cavity (K), we assume that $T_g^* = T_r$.

Since the pneumatic transport conditions may be attained before the reactor outlet, it is assumed that, as soon as equal solids and gas velocities are achieved for the first time, that is, $U_s = U_g$, pneumatic transport starts. In this case, the solids volumetric fraction is given by

$$\varepsilon_s(z) = \frac{\left(\frac{\dot{m}_{CaO}(z)}{\rho_{CaO}} + \frac{\dot{m}_{CaCO_3}(z)}{\rho_{CaCO_3}}\right)}{\left(\frac{\dot{m}_{CaO}(z)}{\rho_{CaO}} + \frac{\dot{m}_{CaCO_3}(z)}{\rho_{CaCO_3}}\right) + \left(\frac{\dot{m}_{CO_2}(z)}{\rho_{CO_2}(z)} + \frac{\dot{m}_{H_2O}(z)}{\rho_{H_2O}(z)}\right)}. \tag{37}$$

2.5. Energy balance equations

An energy balance in a control volume of the reactor for steady-state conditions such as the one in Fig. 1 can be obtained for the bed temperature T_b (K), from the powers per unit of length $\widetilde{H}_{calc}$ and $\widetilde{H}_{w-b}$ for the reaction kinetics and wall-bed heat transfer (W m^{-1}), respectively:

$$\frac{dT_b(z)}{dz} = \frac{1}{\dot{m}_s(z)C_{P,s}(z) + \dot{m}_g(z)C_{P,g}(z)}\left(\widetilde{H}_{w-b}(z) - \widetilde{H}_{calc}(z)\right), \tag{38}$$

with

$$\widetilde{H}_{calc}(z) = \Delta H_{calc}(T_b(z))\, r_{calc}(z)\, A, \tag{39}$$

$$\widetilde{H}_{w-b}(z) = \frac{\pi D}{n_{el}}\sum_{i=1}^{n_{el}} h_{w-b,i}(z)\left(T_{w,i}(z) - T_b(z)\right), \tag{40}$$

where $\Delta H_{calc}(T_b)$ is the enthalpy of $CaCO_3$ calcination reaction at the bed temperature (J mol^{-1}) and $C_{P,s}$ and $C_{P,g}$ are the specific

heat capacities of the solids and gas (J kg^{-1} K^{-1}), computed from the temperature-dependent specific heat capacities $C_{P,i}$ of the individual species i (J kg^{-1} K^{-1}) as

$$\Delta H_{calc}(T_b(z)) = \Delta H_{calc}^0 + \int_{T_{ref}}^{T_b(z)} \sum_{i\in\{CaCO_3,CaO,CO_2\}}\left(\nu_i M_i C_{P,i}(\theta)\right)d\theta, \tag{41}$$

$$C_{P,f}(z) = \frac{\sum_{i\in S_f}\dot{m}_i(z)C_{p,i}\left(T_f(z)\right)}{\dot{m}_f(z)}, \qquad f \in \{s, g\}, \tag{42}$$

D is the reactor diameter (m), n_{el} is the number of elements of the wall in the simulation (-), $T_{w,i}$ is the wall temperature in the ith element (K), and $h_{w-b,i}$ is the total wall-bed HTC in the ith element (W m^{-2} K^{-1}). The first and second terms on the right-hand side of (38) correspond to the heat transfer and source terms in Fig. 1, respectively.

The energy balance equations assume that the solids temperature T_s and the gas temperature T_g are both equal to the bed temperature T_b. To ensure that this assumption is satisfied, one needs to verify that the power per unit of length for the gas–solid heat transfer (W m^{-1}) given by

$$\widetilde{H}_{g-s}(z) = \alpha(z)A(T_g(z) - T_s(z)), \tag{43}$$

where α is the volumetric gas–solid HTC (W m^{-3} K^{-1}), is very large whenever T_s and T_g are different. This can be done, for example, by verifying that the gas–solid HTC per unit of length (W m^{-1} K^{-1}) given by

$$\widetilde{h}_{g-s}(z) = \alpha(z)A, \tag{44}$$

is much larger than the total wall-bed HTC per unit of length (W m^{-1} K^{-1}) given by

$$\widetilde{h}_{w-b}(z) = \frac{\pi D}{n_{el}}\sum_{i=1}^{n_{el}} h_{w-b,i}(z), \tag{45}$$

whenever T_w is varying with z or is different from T_b.

Also, since the inlet solids and gas temperatures may be different, one can define the inlet bed temperature $T_b(0)$ as the temperature of an adiabatic process of mixture of solids and gas such that

$$\int_{T_s(0)}^{T_b(0)}\left(\sum_{i\in S_s}\dot{m}_i(0)C_{p,i}(\theta)\right)d\theta = \int_{T_b(0)}^{T_g(0)}\left(\sum_{i\in S_g}\dot{m}_i(0)C_{p,i}(\theta)\right)d\theta, \tag{46}$$

where $T_b(0)$ is the temperature that the solids and the gas would immediately achieve in the case of very fast gas–solid heat transfer.

The wall-bed heat flux at the ith element (W m^{-2}) is defined as

$$H_{w-b,i}(z) = h_{w-b,i}(z)\left(T_{w,i}(z) - T_b(z)\right). \tag{47}$$

Hence, the wall-bed heat transfer can be written as a function of the total wall-bed HTC $h_{w-b,i}(z)$ and the corresponding temperature difference between the wall and the bed for a given element of the wall. Experiments in CFB risers have shown that the walls are intermittently covered by particle clusters and a dilute gas–solid stream (Basu, 2015). Fig. 3 shows the distribution of solids in the lean zone, including the core and annulus regions and the cluster formation in the annulus region. Several heat transfer mechanisms are present, namely, (1) convection/conduction between clusters and wall through a thin gas film, (2) radiation from clusters, (3) convection, and (4) radiation from the disperse phase. The individual heat transfer mechanisms are summed up to compute a total HTC. To this end, the fraction δ_c of the wall in contact with clusters (-) is considered, while the remaining fraction is in contact with the dilute gas–solid stream. The total HTC between the surface and the fluidized bed is:

$$h_{w-b,i}(z) = \delta_c(z)\left(h_{c,i}(z) + h_{c,rad,i}(z)\right) + (1-\delta_c(z))\left(h_{d,i}(z) + h_{d,rad,i}(z)\right), \tag{48}$$

where the subscripts c, d, and rad refer to the clusters, disperse phase, and radiation (W m^{-2} K^{-1}), respectively.

The time-averaged fraction δ_c of the wall area covered by the clusters can be estimated as

$$\delta_c(z) = \begin{cases} 0 & z \in [0; H_{dense}] \\ \delta_{c,lean}(z) & z > H_{dense} \end{cases}, \tag{49}$$
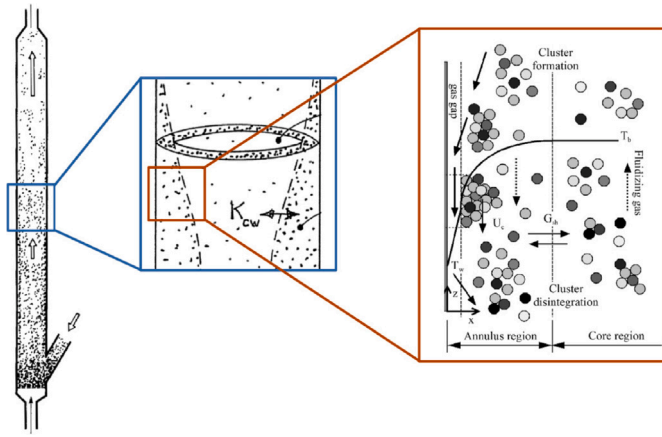
Fig. 3. Distribution of solids in the lean zone of the riser of a CFB, showing the core and annulus regions with the cluster formation over the heat transfer surface.
Source: Adapted from Kunii and Levenspiel (1991), Kunii and Levenspiel (2000), and Błaszczuk (2015).

with

$$\delta_{c,lean}(z) = 0.5 \left(\frac{1 - \varepsilon_{cw}(z) - 0.00001}{1 - \varepsilon_c(z)} \right)^{0.5}, \tag{50}$$

where the gas volumetric fractions within the clusters ε_c (-) and near the wall ε_{cw} (-) are given by (Li et al., 1988; Harris et al., 2002):

$$\varepsilon_c(z) = 0.6, \tag{51}$$

$$\varepsilon_{cw}(z) = \begin{cases} 1 - \varepsilon_s(z) & z \in [0; H_{dense}] \\ 1 - 0.58 \frac{\varepsilon_s(z)^{1.48}}{0.013 + \varepsilon_s(z)^{1.48}} & z > H_{dense} \end{cases}, \tag{52}$$

which empirically expresses the fact that the local volume fraction of solids increases continuously from the center toward the wall in the lean zone.

The wall transfers heat to the upflowing disperse phase between the clusters. The HTC $h_{d,i}$ from a dilute and uniform gas–solid suspension to the wall is given by the approximation (Basu, 2015)

$$h_{d,i}(z) = \frac{k_g C_{P,s}(z)}{d_p C_{P,g}(z)} \left(\frac{\rho_d(z)}{\rho_s(z)} \right)^{0.3} \left(\frac{U_t(z)^2}{g d_p} \right)^{0.21} Pr(z), \tag{53}$$

based on the particle diameter d_p (m), gravity acceleration $g = 9.81$ m s^{-2}, gas thermal conductivity k_g (W m^{-1} K^{-1}), and terminal velocity of particles U_t (m s^{-1}), given by

$$U_t(z) = \frac{\mu_g(z)}{d_p \rho_g(z)} \left(\frac{Ar(z)}{7.5} \right)^{0.666}, \tag{54}$$

with the Archimedes number Ar (-)

$$Ar(z) = \frac{\rho_g(z)(\rho_s(z) - \rho_g(z))g d_p^3}{\mu_g(z)^2}, \tag{55}$$

the gas viscosity μ_g (kg m^{-1} s^{-1}), specific heat capacities $C_{P,g}$ and $C_{P,s}$ and densities ρ_g and ρ_s of gas and solids, as well as the density ρ_d of the disperse phase (kg m^{-3}) that depends on the solids volumetric fraction $\varepsilon_{s,d} = 0.00001$ of the disperse phase near the wall

$$\rho_d(z) = (1 - \varepsilon_{s,d}) \rho_g(z) + \varepsilon_{s,d} \rho_s(z), \tag{56}$$

and the Prandtl number Pr (-)

$$Pr(z) = C_{P,g}(z) \frac{\mu_g(z)}{k_g}. \tag{57}$$

The HTC $h_{d,rad,i}$ of radiation from the disperse phase to the wall is computed as

$$h_{d,rad,i}(z) = \frac{\sigma(T_s(z)^4 - T_{w,i}(z)^4)}{(\frac{1}{e_d} + \frac{1}{e_w} - 1)(T_s(z) - T_{w,i}(z))}, \tag{58}$$

based on the Stefan–Boltzmann constant $\sigma = 5.67 \times 10^{-8}$ W m^{-2} K^{-4}, wall emissivity e_w (-) and the emissivity e_d of the disperse phase (-) considering scattering (Brewster, 1986):

$$e_d = \left[\frac{e_s}{0.5(1 - e_s)} \left(2 + \frac{e_s}{0.5(1 - e_s)} \right) \right]^{0.5} - \frac{e_s}{0.5(1 - e_s)}, \tag{59}$$

which is calculated from the emissivity e_s of the particle surface (-), assuming that the condition

$$e'_p = 1 - \exp\left(-\frac{5.25 e_s Y' D}{\pi d_p} \right) > 0.6 \tag{60}$$

for the effective emissivity e'_p of a particle cloud (-) is satisfied with the solids volumetric fraction $\varepsilon'_s = 0.0064$ in choked condition as mentioned by Basu (2015). For these reasons, radiative heat transfer between particles is implicitly included in the radiative heat transfer between the disperse phase and the wall.

The clusters travel a certain distance, detach from the wall, disintegrate, and form again in the riser. While the clusters are in contact with the wall, they are initially considered at the bed temperature, and then transient heat transfer between the wall and the clusters takes place. The heat transfer from the clusters depends not only on the contact resistance on the wall but also on the conduction resistance of the clusters. The contact resistance equals the thermal resistance of a gas film with a thickness equal to a fraction of the particle diameter (Basu, 2015). Consequently, the HTC $h_{c,i}$ from the clusters to the wall is given by

$$h_{c,i}(z) = \frac{1}{\left(\frac{\pi t_c}{4 k_c(z) \rho_c(z) C_{P,c}} \right)^{0.5} + \frac{d_p}{10 k_{gf,i}(z)}}, \tag{61}$$

depending on the: (i) particle diameter; (ii) average residence time $t_c = 8$ s of clusters on the wall; (iii) thermal conductivity $k_{gf,i}$ of gas (W m^{-1} K^{-1}) evaluated at the mean gas-film temperature $T_{f,i}$ (K)

$$k_{gf,i}(z) = 1.5207 \times 10^{-11} T_{f,i}^3(z) - 4.8574 \times 10^{-8} T_{f,i}^2(z) + 1.0184 \times 10^{-4} T_{f,i}(z) - 0.00039333, \tag{62}$$

$$T_{f,i}(z) = \frac{T_s(z) + T_{w,i}(z)}{2}; \tag{63}$$

(iv) cluster thermal conductivity k_c (W m^{-1} K^{-1})

$$k_c(z) = k_g \left(1 + \frac{(1 - \varepsilon_c(z))\left(1 - \frac{k_g}{k_s} \right)}{\frac{k_g}{k_s} + 0.28 \varepsilon_c(z)^{0.63 \left(\frac{k_s}{k_g} \right)^{0.18}}} \right) \tag{64}$$

that depends on the thermal conductivities k_g and k_s of gas and solids (W m^{-1} K^{-1}); (v) cluster specific heat capacity $C_{P,c}$ (J kg^{-1} K^{-1})

$$C_{P,c}(z) = (1 - \varepsilon_c(z)) C_{P,s}(z) + \varepsilon_c(z) C_{P,g}(z); \tag{65}$$

and (vi) cluster density ρ_c (kg m^{-3})

$$\rho_c(z) = (1 - \varepsilon_c(z)) \rho_s(z) + \varepsilon_c(z) \rho_g(z). \tag{66}$$

The HTC $h_{c,rad}$ of radiation from the clusters to the wall is computed as

$$h_{c,rad,i}(z) = \frac{\sigma(T_{c,i}(z)^4 - T_{w,i}(z)^4)}{(\frac{1}{e_c} + \frac{1}{e_w} - 1)(T_{c,i}(z) - T_{w,i}(z))}, \tag{67}$$

based on the cluster emissivity e_c (-) considering multiple reflections of particles (Grace, 1984)

$$e_c = 0.5(1 + e_s), \tag{68}$$

as well as the cluster temperature $T_{c,i}$ (K)

$$T_{c,i}(z) = T_{w,i}(z) + 1.29 \left(\frac{\rho_{susp}(z)}{\rho_s(z)} \right)^{0.13} (T_s(z) - T_{w,i}(z)), \quad (69)$$

where the average suspension density ρ_{susp} (kg m^{-3}) is (Dutta and Basu, 2005)

$$\rho_{susp}(z) = \varepsilon_s(z)\rho_s(z) + \varepsilon_g(z)\rho_g(z). \quad (70)$$

The volumetric gas–solid HTC is given by Kuipers et al. (1992)

$$\alpha(z) = \frac{6(1 - \varepsilon_g(z))\alpha_p(z)}{d_p}, \quad (71)$$

which equals the product of the specific interfacial area and the gas-particle HTC α_p (W m^{-2} K^{-1})

$$\alpha_p(z) = \frac{Nu_p(z)k_g}{d_p}, \quad (72)$$

where the particle Nusselt number Nu_p (-) is estimated from a correlation (Xie et al., 2003)

$$Nu_p(z) = 2 + 1.8 Re_p(z)^{0.5} Pr(z)^{1/3}, \quad (73)$$

and the particle Reynolds number Re_p (-) is given by

$$Re_p(z) = \varepsilon_g(z)\rho_g(z)(U_g(z) - U_s(z)) \frac{d_p}{\mu_g(z)}, \quad (74)$$

where $U_g(z) - U_s(z)$ represents the gas velocity with respect to the solid particles.

The environment-wall heat flux $H_{e-w,i}$ at the ith wall element (W m^{-2}) is given by

$$H_{e-w,i}(z) = H_{irr,i}(z) - h_{r,rad,i}(z)(T_{w,i}(z) - T_r)$$
$$+ k_w d_w \left(\frac{\pi D}{n_{el}} \right)^{-2} (T_{w,i+1}(z) + T_{w,i-1}(z) - 2T_{w,i}(z)), \quad (75)$$

which depends on the concentrated solar irradiance $H_{irr,i}$ on the element (W m^{-2}), as well as the conduction in the wall with a thermal conductivity k_w (W m^{-1} K^{-1}) and a thickness d_w (m), and the HTC $h_{r,rad,i}$ of radiation from the receiver cavity (W m^{-2} K^{-1}), assumed at a uniform temperature T_r as mentioned in Section 2.2, given by

$$h_{r,rad,i}(z) = \frac{\sigma(T_r^4 - T_{w,i}(z)^4)}{(\frac{2}{e_w} - 1)(T_r - T_{w,i}(z))}. \quad (76)$$

The concentrated solar irradiance $H_{irr,i}$ on the ith wall element and the temperature T_r of the receiver cavity correspond to the only boundary conditions that are imposed in the energy balance model in addition to the inlet temperatures. The assumption of a uniform temperature of the receiver cavity is necessary to avoid computing form factors for each axial position on the reactor and the temperature of each point of the receiver cavity, which would require the simulation of the cavity coupled with the solar field in addition to the reactor. Heat loss due to convection from the reactor to its surroundings is neglected since it is expected to be negligible in comparison to the radiative heat loss in a receiver cavity with a small aperture, where the air around the reactor is expected to move at low speeds.

Recall that the wall-bed heat flux $H_{w-b,i}(z)$ at the same element is given by (47). However, note that there is no explicit model equation to compute the temperature $T_{w,i}(z)$. Hence, an iterative procedure for computing the wall temperature was created using the equations for the HTC. These equations depend on the bed temperature, which is used as an input, and the wall temperature, which is to be found. Therefore, the wall temperature $T_{w,i}(z)$ is computed at each step by using an initial guess and iterating until the following equation is satisfied:

$$H_{e-w,i}(z) = H_{w-b,i}(z), \quad (77)$$

which must hold since no heat accumulation takes place in the wall at steady state. Appendix A specifies the iterative method used to determine $T_{w,i}(z)$. Fig. 4 shows a schematic of the heat transfer mechanisms that affect a wall element.
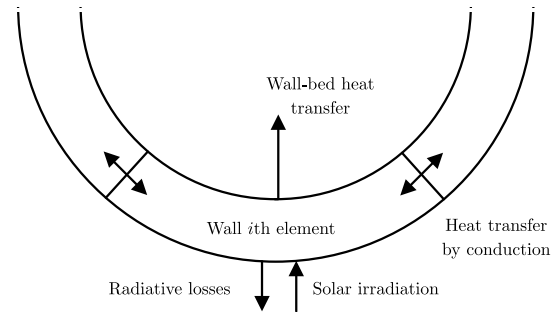

Fig. 4. Schematic of the heat transfer mechanisms that affect a wall element.

Table 1
Reactor parameters.

Parameter	Value	Units
D	0.1	m
H_t	8	m
d_w	0.01	m
e_w	0.8	–
P	120	kPa
T_r	900	°C

Table 2
Solid-gas flow parameters.

Solids			Gas		
Parameter	Value	Units	Parameter	Value	Units
ρ_{CaCO_3}	1320.3	kg m^{-3}	M_{CO_2}	0.044	kg mol^{-1}
ρ_{CaO}	870.5	kg m^{-3}	M_{H_2O}	0.018	kg mol^{-1}
M_{CaCO_3}	0.100	kg mol^{-1}	R_{CO_2}	188.9	J kg^{-1} K^{-1}
M_{CaO}	0.056	kg mol^{-1}	R_{H_2O}	461.7	J kg^{-1} K^{-1}
d_p	300	μm			
e_s	0.9	–			

2.6. Reactor performance indicators

One of the objectives of the model is to predict the reactor performance. For this purpose, the molar calcination conversion η_{calc} (-) is the fraction of CaCO$_3$ converted in the reactor and is computed as

$$\eta_{calc}(z) = \frac{X_{CaCO_3}(0) - X_{CaCO_3}(z)}{X_{CaCO_3}(0)}, \quad (78)$$

in particular for the total reactor height H_t (m).

The conversion of the reactor is correlated with the solids residence time t_s (s). It is expected that, the longer the residence time is, the higher the conversion is. Hence, the residence time of solids can be computed as:

$$\frac{dt_s(z)}{dz} = \frac{1}{U_s(z)}, \qquad t_s(0) = 0. \quad (79)$$

The conversion is also correlated with the maximum temperature reached by the reactor wall. It is expected that, the higher the temperature is, the higher the conversion is. Hence, the maximum mean wall temperature (K) can be computed as:

$$\bar{T}_w = \max_z \frac{1}{n_{el}} \sum_{i=1}^{n_{el}} T_{w,i}(z). \quad (80)$$

2.7. Model parameters

The input parameters of the model are described in this section. Table 1 describes the parameters related to the reactor, while Table 2 describes the parameters related to the solid–gas flow.

The reactor diameter and height were chosen based on current lab-scale CaL systems. The diameter ranges from 0.07–0.1 m for systems with thermal powers between 10–30 kW. Similarly, the reactor

length for lab-scale calciners is in the range of 6–12 m. The reference values for design are 0.1 m diameter and 8 m height, and the final recommendation for the height is based on the simulation results.

It was assumed that the wall is made of AISI 310S stainless steel, which was used as reference material to select an emissivity of 0.8 (Sans et al., 2018). This type of steel was used for the absorber tube receiver on the experimental setup for an on-sun test on a unit at the 1 MW solar furnace of CNRS in Odeillo Font-Romeu (Zhang et al., 2016).

The operation of the reactor occurs approximately at atmospheric pressure. A pressure of 120 kPa was chosen for the reference case. From experimental data, it was checked that the static pressure inside the reactor due to the particles can be neglected (Bidwe, 2017).

A constant temperature of the receiver cavity of 900 °C was chosen since it is expected that the temperature of the receiver cavity and the temperature of the non-irradiated wall tend to similar values and 900 °C corresponds to a temperature above which sintering of the particles becomes particularly important (Erans et al., 2016).

A concentrated solar irradiance distribution $H_{irr,i}(z)$ that depends on both the axial position z and the angular position corresponding to the ith element was selected. This irradiance is given by the product of the sum of two Gaussian curves in the axial direction and a Gaussian curve in the angular direction, which simulates a multiple-point aiming strategy along a vertical axis on the reactor wall. This strategy spreads the irradiance by aiming at different focal points along the centerline of the receiver. More specifically, the irradiance is as follows:

$$H_{irr,i}(z) = \left(8000 \exp\left(-\frac{1}{2}\left(\frac{z-1}{1} \right)^2 \right) + 4000 \exp\left(-\frac{1}{2}\left(\frac{z-2.3}{0.7} \right)^2 \right) \right) \frac{f_i}{\pi D/n_{el}},$$
(81)

where

$$f_i = \begin{cases} \frac{1}{2}\left(\mathrm{erf}\left(\frac{-5+10i/n_{el}}{\sqrt{2}} \right) + 1 \right), & i = 1 \\ \frac{1}{2}\left(\mathrm{erf}\left(\frac{-5+10i/n_{el}}{\sqrt{2}} \right) - \mathrm{erf}\left(\frac{-5+10(i-1)/n_{el}}{\sqrt{2}} \right) \right), & i = 2, \dots, n_{el}-1, \\ \frac{1}{2}\left(1 - \mathrm{erf}\left(\frac{-5+10(i-1)/n_{el}}{\sqrt{2}} \right) \right), & i = n_{el} \end{cases}$$
(82)

and erf is the error function.

Fig. 5 shows the concentrated solar irradiance used in the simulation studies for the reference case as a function of the height and angular position. The irradiance is not zero at the reactor inlet ($z = 0$). Otherwise, if a centered distribution had been used, the required height would significantly increase since a significant reactor height would be needed to heat up the reactant so that the reaction can proceed. However, this is just an example of a non-uniform irradiance that includes a zone with higher intensity, and the exact distribution depends on the control strategy of the solar field and the reactor design, among other factors.

The solids densities were measured in our laboratory using sorbent with a particle diameter between 250–350 μm. The $CaCO_3$ density measurement was done using a fresh sample. For the measurement of CaO density, a sample resulting from the calcination reaction (after one cycle) was used. Calcination was performed in a lab-scale fixed bed reactor, as described by Teixeira et al. (2020). A particle diameter of 300 μm was selected for the reference case. A sensitivity study is performed over the particle range $d_p \in [200; 400]$ μm to assess its effect on the process conversion. The emissivity of limestone was selected to describe the emissivity of the solids in the model. A value of 0.9 was chosen (Craig, 2010).

Table 3 presents the equations used for the calculation of the specific heat capacity of the involved species as a function of the temperature.

The gas dynamic viscosity in kg m^{-1} s^{-1} is computed as the simple mass average given that the individual dynamic viscosity of H_2O and
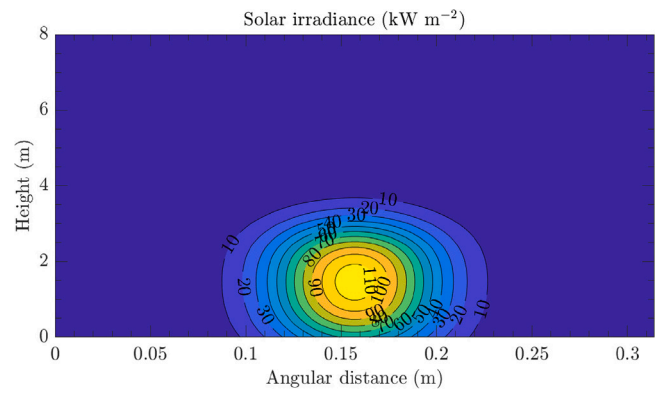

Fig. 5. Concentrated solar irradiance as a function of the calciner height and angular distance.

Table 3
Specific heat capacity of the species (Zeneli et al., 2017).

Validity range of temperature (K)	Specific heat capacity (J kg^{-1} K^{-1})
$298 < T_g \leq 2000$	$C_{p,CO_2} = 535.4 + 1.279T_g - 5.468 \times 10^{-4}T_g^2 - 2.382 \times 10^{-7}T_g^3 + 1.892 \times 10^{-10}T_g^4$
	$C_{p,H_2O} = 1938 - 1.181T_g + 3.644 \times 10^{-3}T_g^2 - 2.863 \times 10^{-6}T_g^3 + 7.596 \times 10^{-10}T_g^4$
$298 < T_s \leq 1000$	$C_{p,CaCO_3} = -147.0097 + 5.14113T_s - 7.33 \times 10^{-3}T_s^2 + 3.83712 \times 10^{-6}T_s^3 - 2.482 \times 10^{-10}T_s^4$
	$C_{p,CaO} = 251.1235 + 2.69093T_s - 4.2066 \times 10^{-3}T_s^2 + 3.0414 \times 10^{-6}T_s^3 - 8.181 \times 10^{-10}T_s^4$
$1000 < T_s \leq 1200$	$C_{p,CaCO_3} = 1199.445 - 0.1161T_s + 1.69741 \times 10^{-4}T_s^2$
	$C_{p,CaO} = 838.5397 + 0.15071T_s - 3.7921 \times 10^{-5}T_s^2 + 8.08248 \times 10^{-9}T_s^3 - 6.313 \times 10^{-13}T_s^4$

Table 4
Parameters of the fluid dynamics model in the reference case and in the sensitivity study.

Parameter	Value (reference)	Range (sensitivity)	Units
a_0	6	[4; 12]	s^{-1}
H_{dense}	0.25	[0; 1]	m

CO_2 are almost the same for the temperature range expected in the reactor:

$$\mu_g = \left(0.0122 + 3.6 \times 10^{-5}\left(T_g - 273.15 \right) \right) \times 10^{-3}.$$
(83)

The thermal conductivities for the solids, the gas, and the reactor wall are $k_s = 0.62$ W m^{-1} K^{-1}, $k_g = 0.10950$ W m^{-1} K^{-1}, and $k_w = 26.0$ W m^{-1} K^{-1}, respectively.

As discussed in previous sections, to model the fluid dynamics two parameters must be selected (Table 4): the height of the dense zone and the decay factor.

A value of 0.25 m was selected for the height of the dense bed in the reference case. According to experimental data from low-density CFBs, which correspond to the reactor described in this work (Bidwe, 2017; Charitos et al., 2011; Xu et al., 2018; Collado, 2016), a bed of some tens of centimeters or even inexistent is expected. Nevertheless, this parameter is likely to affect greatly the calcination conversion of the reactor, thus this input is evaluated in a sensitivity study by varying its value over the range of $H_{dense} \in [0; 1]$ m.

The decay factor is presented in the literature as dependent on a constant superficial gas velocity. The reference value of $\frac{a_0}{U_0(H_{dense})}$ in m^{-1} with $a_0 = 6$ s^{-1} was selected based on the experimental results presented by Kunii and Levenspiel (1991). Later, a sensitivity study is performed for $a_0 \in [4; 12]$ s^{-1}.

Table 5
Boundary conditions of the model in the reference case and in the sensitivity study.

Condition	Value (reference)	Range (sensitivity)	Units
$\dot{m}_s(0)$	0.01	[0.005; 0.025]	kg s^{-1}
$\dot{m}_g(0)$	0.01	[0.005; 0.025]	kg s^{-1}
$w_{CaO}(0)$	0.05	[0; 0.4]	–
$w_{CO_2}(0)$	0	[0; 0.4]	–
$T_s(0)$	600	[300; 800]	°C
$T_g(0)$	650	$T_s(0) + [0; 100]$	°C

2.8. Boundary conditions

The boundary conditions of the model are described in this section. Table 5 presents the boundary conditions of the model. The solids and gas mass flow rates were selected after reviewing the available information on calciners for the CaL process and their cold model studies. The solids circulation rate and the superficial gas velocity ranged from 0.6–5 kg m^{-2} s^{-1} and 2–6 m s^{-1}, respectively (Arias et al., 2018; Ylätalo, 2013; Martínez et al., 2011). This corresponds to solids and gas flow rates around 0.01 kg s^{-1}, which was chosen as the value for the reference conditions. It must be noted that the operating conditions of reactors are given in literature based on constant solids circulation rates and superficial gas velocities. In contrast, in this model, the superficial gas velocity is calculated and not introduced as an input. A sensitivity study for $\dot{m}_g(0)$ and $\dot{m}_s(0)$ is presented in the upcoming sections. The variation range is $\dot{m}_g(0) \in [0.005; 0.025]$ kg s^{-1} and $\dot{m}_s(0) \in [0.005; 0.025]$ kg s^{-1}.

The inlet mass fractions of CaO and CO$_2$, $w_{CaO}(0)$ and $w_{CO_2}(0)$, were also chosen to match typical experimental conditions according to the literature. In the beginning, fresh CaCO$_3$ without any content of CaO is expected to be used. After the first cycle, the inlet stream of solids corresponds to the one recovered from the carbonator, which has a higher content of CaO due to the deactivation of the sorbent. Teixeira et al. (2020) concluded that the fraction of unreacted CaO is highly dependent on the type of sorbent used. It was found that, for CaO precursors such as dolomite, the fraction of unreacted CaO after one cycle was much lower (5%–8%) when compared with wastes of marble powder (20%–30%). Therefore, a reference value for the inlet mass fraction of CaO of 5% is selected. A sensitivity study is conducted for a range of values of $w_{CaO}(0) \in [0; 0.4]$. Similarly, the inlet mass fraction of CO$_2$ selected for the reference case is 0. From the literature, it is known that a high local concentration of CO$_2$ reduces the reaction rate. Therefore, a sensitivity study is performed for the inlet mass fractions of CO$_2$ for typical values $w_{CO_2}(0) \in [0; 0.4]$ found in the literature (Fernandez et al., 2019).

The inlet bed temperature was assumed to be approximately 650 °C as this is a typical temperature at the carbonator outlet in CaL processes for CO$_2$ capture (Teixeira et al., 2019) and is expected to be similar to the temperature after the carbonator and corresponding heat exchanger network in CaL processes for TCES (Ortiz et al., 2018). On the other hand, the solids temperature is slightly lower (600 °C) than the gas temperature (650 °C) to check what happens when thermal equilibrium between the two phases occurs. However, depending on the conditions for storage of the carbonation products, the temperatures in the process for TCES may be lower. Therefore, the need for preheating of the sorbent and the fluidizing gas is also assessed in the sensitivity study ($T_s(0) = [300; 800]$ °C and $T_g(0) - T_s(0) = [0; 100]$ °C).

3. Results and discussion

This section shows and discusses the simulation results obtained with the model in Section 2. Section 3.1 discusses the results for the reference conditions in greater detail, in particular for the case of imposed concentrated solar irradiance (labeled as irradiance in the remainder of this section) with wall conduction in the angular direction. As shown in
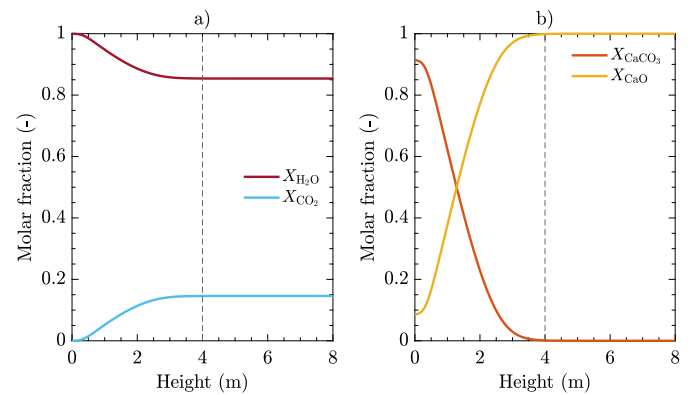

Fig. 6. Molar fractions of the (a) gas species and (b) solid species as a function of the calciner height for the case of imposed irradiance with wall conduction in the angular direction.
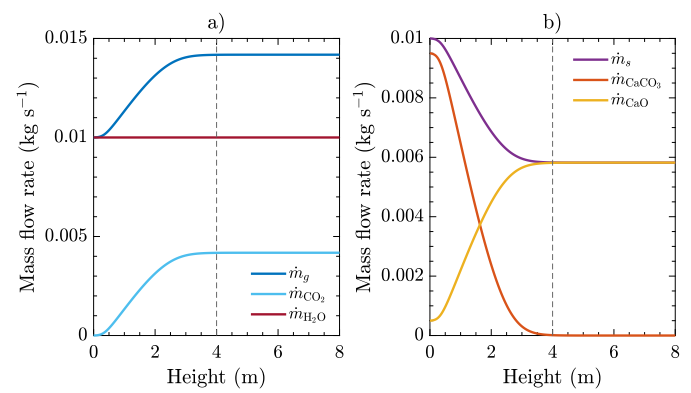

Fig. 7. Mass flow rates of the (a) gas species and (b) solid species as a function of the calciner height for the case of imposed irradiance with wall conduction in the angular direction.

Section 3.2, the results for imposed irradiance without wall conduction in the angular direction or with fewer wall elements are very similar. Then, Section 3.3 presents a sensitivity analysis with respect to several model parameters and operating conditions. All the simulations were performed on MATLAB R2020a running on a 1.8 GHz Intel Core i7 processor. The MATLAB function ode23s was used to solve the ordinary differential equations of the model and to automatically determine the mesh in the axial direction.

3.1. Results for reference conditions

The detailed results for the reference conditions are presented next.

3.1.1. Molar fractions and mass flow rates

Fig. 6 shows the gas and solids molar fractions as a function of the calciner height, while Fig. 7 shows the gas and solids mass flow rates. Both figures show that the solid CaCO$_3$ at the reactor inlet is fully converted to solid CaO and gaseous CO$_2$. This increases the gas mass flow rate and decreases the solids mass flow rate along the reactor. The increase in gas mass flow rate is exclusively due to a larger mass flow rate of CO$_2$, which increases from a molar fraction of 0 to around 0.15. The solids, which are mostly composed of CaCO$_3$ and contain a molar fraction of CaO lower than 0.10 at the reactor inlet, are fully converted to CaO after a height of approximately 4 m.
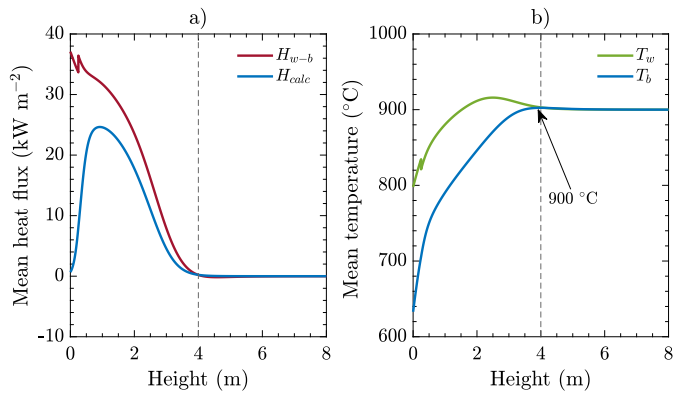
Fig. 8. (a) Mean heat fluxes and (b) mean wall and bed temperatures as a function of the calciner height for the case of imposed irradiance with wall conduction in the angular direction.
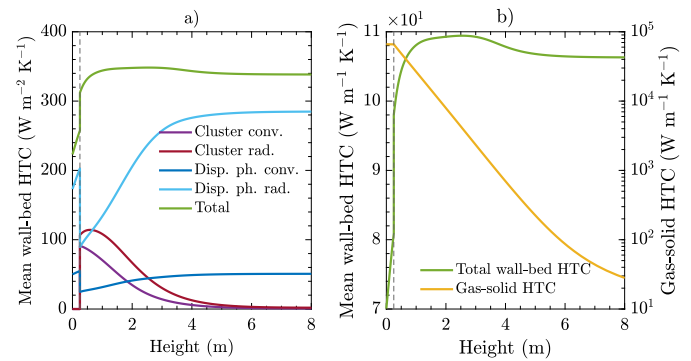

Fig. 9. (a) Mean wall-bed heat transfer coefficients to the disperse phase and clusters and (b) mean total wall-bed and gas–solid heat transfer coefficients per unit of height as a function of the calciner height for the case of imposed irradiance with wall conduction in the angular direction.
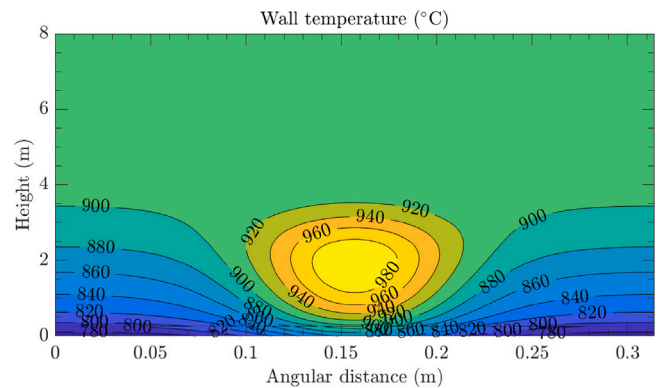

Fig. 10. Wall temperature as a function of the calciner height and angular distance for the case of imposed irradiance with wall conduction in the angular direction.

3.1.2. Heat transfer and temperatures

Fig. 8 shows the mean heat fluxes and the mean temperatures at each axial position. Note that the wall temperature and the wall-bed heat flux depend not only on the axial position but also on the angular position on the wall, which explains the need to define mean quantities with respect to the angular position. The results for the heat flux show the following facts: (i) the wall-bed heat flux H_{w-b} is larger than the calcination heat flux H_{calc} in the initial 4 m of the reactor; (ii) the heat fluxes almost tend to zero after a height of approximately 4 m, including the calcination heat flux, which is a result of the imposed irradiance that approaches zero around that height and confirms that the reaction no longer takes place beyond that position. In addition, the results for the temperature show the following facts: (i) the wall temperature remains approximately 100 °C higher than the bed temperature near the reactor inlet and becomes almost equal to the bed temperature after approximately 4 m, where this temperature reaches a maximum of around 900 °C; (ii) the temperatures tend to the temperature of the reactor cavity at around 900 °C. From these results, it is possible to infer that: (i) the wall-bed heat flux is necessary to provide the heat flux required for the calcination reaction and to increase the bed temperature from less than 650 °C up to around 900 °C; (ii) the maximum bed temperature of around 900 °C may cause sintering of CaO, which may require future work to ensure that the temperature does not increase beyond this value by using an aiming strategy for the solar field that allows a spatially homogeneous irradiance; and (iii) it is the bed temperature after thermal equilibrium that is reached near the reactor inlet, rather than the set of both inlet gas and solids temperatures, that determines the temperature profile in the reactor.

Fig. 9 presents the wall-bed HTC to the disperse phase and clusters for both conduction and radiation transfer mechanisms, as well as the total wall-bed HTC. Once again, a mean HTC is shown since each coefficient varies not only in the axial direction but also in the angular direction. Due to the existence of a dense bed in the initial part of the reactor with a height of $H_{dense} = 0.25$ m and according to the model assumption that the dense bed behaves as a disperse phase without clusters, the fraction of clusters on the wall is zero and only heat transfer to the disperse phase takes place. Then, in the lean zone beyond the height of 0.25 m, heat transfer to the clusters also occurs and causes a discontinuity in the total HTC by taking into account the fraction of clusters on the wall, which explains the discontinuity in Figs. 8 and 9 at a height of 0.25 m. In the lean zone, the total HTC increases until it reaches a maximum value of around 350 W m^{-2} K^{-1} at a height of approximately 3 m. Beyond that axial position, the total HTC gradually decreases and reaches a value of around 340 W m^{-2} K^{-1} at the reactor outlet. The total HTC varies from 210 to 350 W m^{-2} K^{-1}, which is

in the range of values suggested in the literature for CFBs. The most significant heat transfer mechanism in all the axial positions except between a height of 0.25 m and 0.75 m is radiation to the disperse phase, with a coefficient that reaches a maximum value of around 280 W m^{-2} K^{-1} and significantly increases in the lean zone. The HTC to the clusters decreases almost everywhere between the beginning of the lean zone and the reactor outlet, which is a result of smaller fractions of the wall covered by clusters as one moves up in the axial direction, while the HTC of convection to the disperse phase slightly increases in that zone.

To gain further insight into the wall-bed heat transfer phenomena, Figs. 10, 11, and 12 show the dependence of the wall temperature, wall-bed heat flux, and total wall-bed HTC not only on the reactor height but also on the angular distance. Due to the imposed irradiance with a maximum at the center of the tube (angular distance of 0.157 m) as seen in Fig. 5, the aforementioned quantities reach their maximum at that angular distance for each value of reactor height. More specifically, the wall temperature and the total wall-bed HTC reach their maximum of more than 980 °C and more than 380 W m^{-2} K^{-1} at a reactor height around 2 m, respectively. On the other hand, the wall-bed heat flux reaches its maximum of more than 60 kW m^{-2} at a reactor height around 1 m, although the mean wall-bed heat flux is larger at smaller reactor heights due to the lower gas and solids temperatures, as seen in Fig. 8.

3.1.3. Volumetric fractions

Fig. 13 presents the solids volumetric fraction ε_s, the fraction δ_c of wall covered by clusters, the gas velocity U_g, the solids velocity U_s, and the superficial gas velocity U_0. After the initial part of the reactor
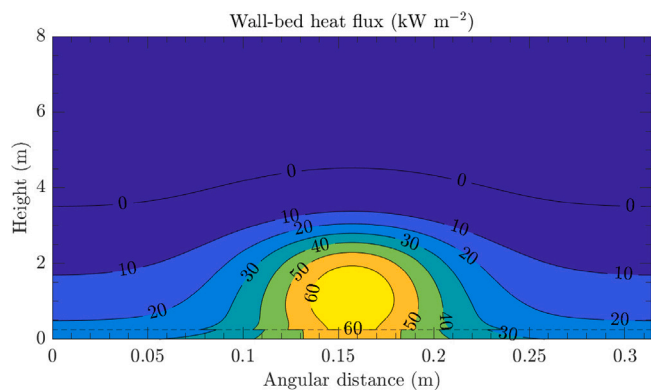
Fig. 11. Wall-bed heat flux as a function of the calciner height and angular distance for the case of imposed irradiance with wall conduction in the angular direction.
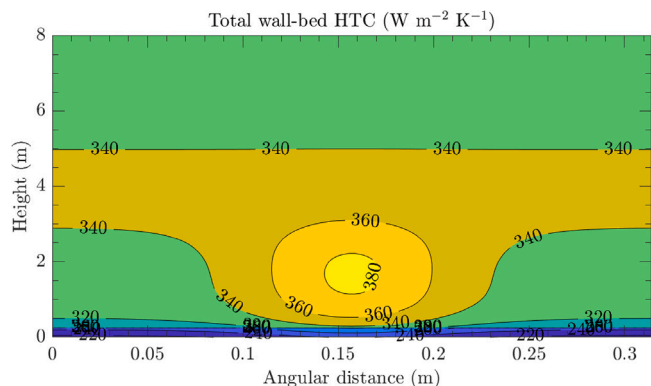

Fig. 12. Total wall-bed heat transfer coefficient as a function of the calciner height and angular distance for the case of imposed irradiance with wall conduction in the angular direction.
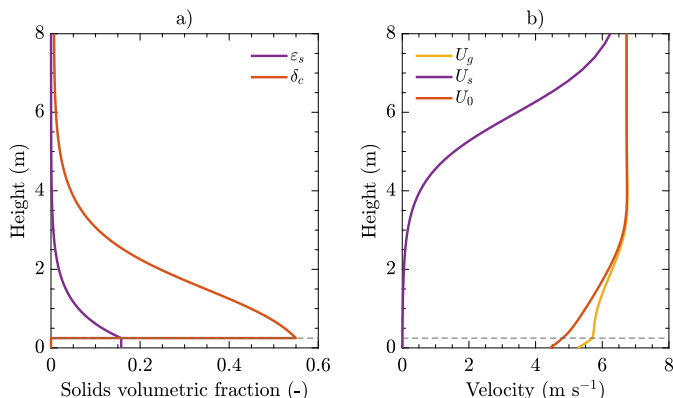

Fig. 13. (a) Solids volumetric fraction and fraction of the wall covered by clusters and (b) gas and solids velocities as a function of the calciner height for the case of imposed irradiance with wall conduction in the angular direction.

Fig. 14. (a) Reaction rate and quantities that affect it ((b) kinetic constant, (c) CO_2 concentrations, and (d) solids concentration) as a function of the calciner height for the case of imposed irradiance with wall conduction in the angular direction.

Fig. 15. (a) Residence time of solids and (b) molar calcination conversion as a function of the calciner height for the case of imposed irradiance with wall conduction in the angular direction.

that corresponds to the dense bed, where ε_s is constant and $\delta_c = 0$, the fractions ε_s and δ_c follow a similar decreasing trend in the lean zone, which results from the relationship between these two variables. As a consequence, the solids velocity starts at a minimum value and increases along the reactor, until it almost converges to the values of the gas velocity and superficial gas velocity at the reactor outlet. The small difference between the gas velocity and the superficial gas velocity in the initial part of the reactor is related to their definition since the gas velocity considers the volumetric fraction occupied by the gas phase
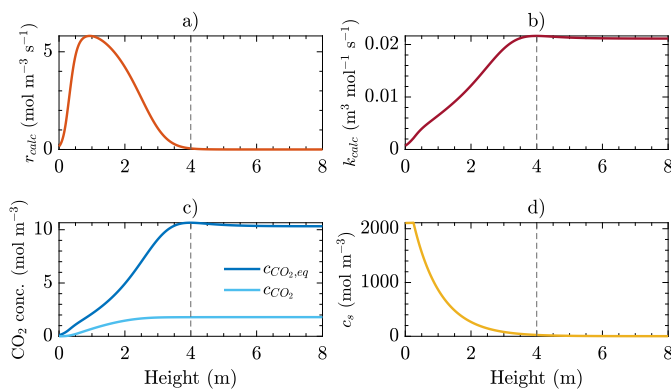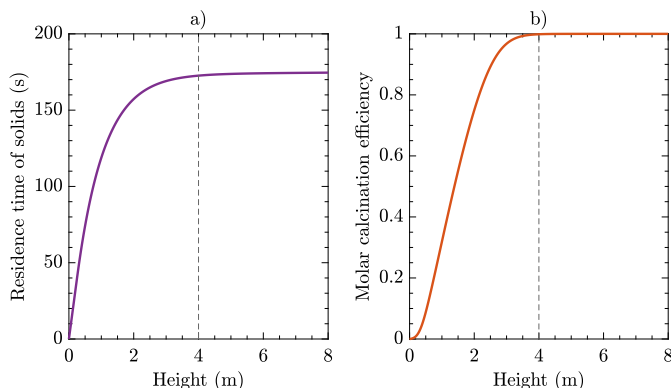
in each reactor section, while the superficial gas velocity considers the whole section. Figs. 7, 8 and 13 show that the typical assumption of constant densities, constant superficial gas velocity, and constant mass flow rates when the K-L fluid dynamics model is used is not suitable for modeling of high-temperature reactive systems such as a solar calciner. For example, in the case of the superficial gas velocity, it increases in the first 4 m of the reactor due to the smaller gas densities caused by higher temperatures and the larger gas mass flow rates caused by the release of CO_2. This justifies the proposed adaptation of the K-L model in a way that considers the varying temperature and mass flow rate.

3.1.4. Reaction rate

Fig. 14 shows the reaction rate and the quantities that it depends on along the reactor height. While the kinetic constant k_{calc} and the difference between equilibrium and local CO_2 concentrations reach their maxima of around 0.02 m^3 mol^{-1} s^{-1} and 10 mol m^{-3}, respectively, at a height of approximately 4 m, the reaction rate r_{calc} reaches its maximum of around 6 mol m^{-3} s^{-1} at a height of approximately 1 m. This is caused by the decreasing solids concentration c_s, which changes from around 2000 mol m^{-3} at the reactor inlet to almost zero at the reactor outlet due to the increasing solids velocity and decreasing solids volumetric fraction.

3.1.5. Residence time and molar calcination conversion

Fig. 15 shows the residence time of solids and the molar calcination conversion as a function of the calciner height. Regarding the residence time of solids, it can be observed that the solids spend almost all their residence time in the first 3–4 m of the reactor. Note that most of the
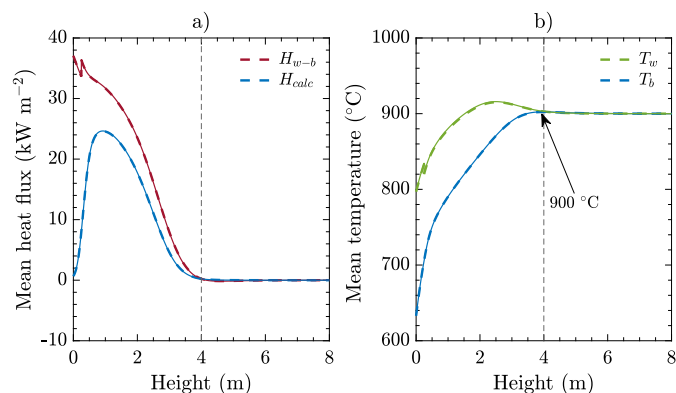
Fig. 16. (a) Mean heat fluxes and (b) mean wall and bed temperatures as a function of the calciner height for the case of imposed irradiance without wall conduction in the angular direction (thick dashed lines), compared with the results for the case of imposed irradiance with wall conduction in the angular direction (thin solid lines).

Fig. 17. Maximum mean wall temperature as a function of the number of elements for the case of imposed irradiance without wall conduction in the angular direction.

calcination reaction also takes place in that part of the reactor. In fact, the trends that are observed for the molar calcination conversion and the residence time of solids are similar since their variation depends linearly on the inverse of the solids velocity. The possible selection of a relatively short height of around 4 m for the reactor is supported by the following observations: (i) the curve for the residence time of solids flattens after 4 m as shown by Fig. 15; and (ii) the curve for the reaction rate also flattens after the same height according to Fig. 14.

3.2. Effect of model features

3.2.1. Effect of gas–solid heat transfer

As mentioned, the proposed model relies on the assumption that the gas and solids temperatures tend instantaneously to the same temperature near the reactor inlet. The simulation results in Figs. 8 and 9 show that the gas–solid HTC is much larger than the total wall-bed HTC in the first 4 m of the reactor, where the temperatures are varying with the height. This supports the assumption that the difference between gas and solids temperatures is negligible in comparison with the difference between these temperatures and the wall temperature, thus the bed temperature at a given height can be considered uniform.

3.2.2. Effect of wall conduction in the angular direction

The simulation results were also obtained for the case of imposed irradiance without wall conduction in the angular direction, which is presented in Fig. 16. The figure shows that all the heat fluxes and temperatures are very similar to the ones for the case with wall conduction in the angular direction. However, the computation time is significantly larger for the case with wall conduction in the angular direction, namely, almost 20 s, compared to around 2 s for the case without wall conduction in the angular direction. Hence, the case without wall conduction in the angular direction is more convenient for extensive simulations with the model in the present paper and is used in the remainder of the paper, particularly for sensitivity analysis.

3.2.3. Effect of the number of wall elements

Fig. 17 shows how the maximum mean wall temperature varies for different values of the number n_{el} of wall elements considered in the simulation. Regarding the molar calcination conversion, it is always equal to 1 independently of the number of elements. The maximum mean wall temperature exhibits a slight variation with the number of elements. More specifically, this variation is less than 0.5 °C when the number of elements is increased from 3 to 100. The maximum mean wall temperature remains almost constant when the number of elements is varied from 30 to 100, thus no benefit in the simulation accuracy is expected if the number of elements is increased above 100.
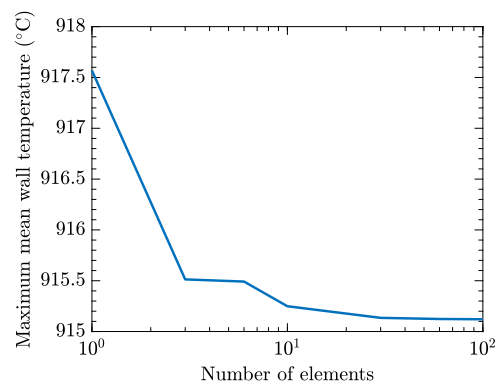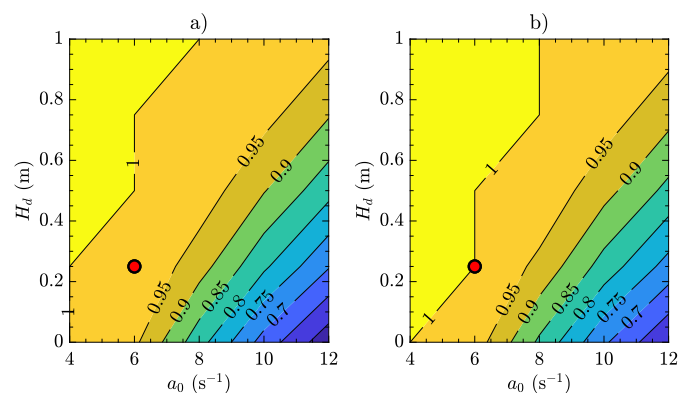

Fig. 18. Molar calcination conversion at reactor heights of (a) 4 m and (b) 6 m as a function of the decay factor and dense bed height for the case of imposed irradiance without wall conduction in the angular direction. The nominal parameter values are indicated by a red circle with a black edge. (For interpretation of the references to color in this figure legend, the reader is referred to the web version of this article.)

3.3. Sensitivity analysis

Next, a sensitivity analysis for various model parameters and operating conditions is performed to check their effect on the molar calcination conversion at two reactor heights, 4 m and 6 m, for the case of imposed irradiance without wall conduction in the angular direction. The results of this analysis are not shown for the other model parameters such as the particle diameter since their effect on the molar calcination conversion is negligible.

3.3.1. Effect of the parameters of the fluid dynamics model

Fig. 18 shows the molar calcination conversion for different values of the decay factor and dense bed height around the nominal values of these parameters of the fluid dynamics model. It can be observed that the molar calcination conversion has a relatively strong dependence on these parameters and the highest values of molar calcination conversion are achieved for small values of the decay factor and large values of the dense bed height. For both parameters, the reasons for this trend are the same: a small decay factor and a large dense bed height result in a large solids volumetric fraction in a larger region of the reactor near the inlet, leading to a small solids velocity and a large residence time in that region where reaction takes place. This sensitivity analysis supports the need to perform experimental tests in high-temperature reactive systems with the goal of estimating accurate parameters for the fluid dynamics model, which may require measuring the solids volumetric fraction along the reactor height.
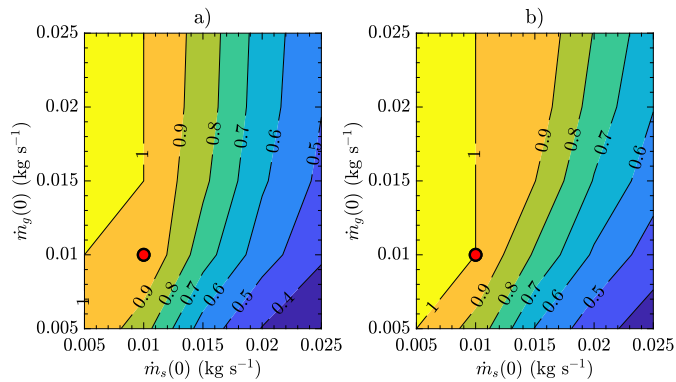
Fig. 19. Molar calcination conversion at reactor heights of (a) 4 m and (b) 6 m as a function of the inlet gas and solids mass flow rates for the case of imposed irradiance without wall conduction in the angular direction. The nominal operating conditions are indicated by a red circle with a black edge. (For interpretation of the references to color in this figure legend, the reader is referred to the web version of this article.)

Fig. 20. Molar calcination conversion at reactor heights of (a) 4 m and (b) 6 m as a function of the inlet mass fractions of CO_2 and CaO for the case of imposed irradiance without wall conduction in the angular direction. The nominal operating conditions are indicated by a red circle with a black edge. (For interpretation of the references to color in this figure legend, the reader is referred to the web version of this article.)

Fig. 21. Molar calcination conversion at reactor heights of (a) 4 m and (b) 6 m as a function of the inlet gas and solids temperatures for the case of imposed irradiance without wall conduction in the angular direction. The nominal operating conditions are indicated by a red circle with a black edge. (For interpretation of the references to color in this figure legend, the reader is referred to the web version of this article.)

3.3.2. Effect of the inlet mass flow rates

Fig. 19 presents the molar calcination conversion for different values of inlet gas and solids mass flow rates around the nominal operating conditions. Even for the smallest gas mass flow rates of 0.005 kg s^{-1}, the gas velocity is larger than 2 m s^{-1}, which allows achieving a low-density fast fluidization regime (Sun and Zhu, 2019). It can be observed that the best operating region for a higher molar calcination conversion corresponds to large inlet gas mass flow rates and small inlet solids mass flow rates. However, for the application of solar calciners to the CaL-TCES process, in principle it would be preferable to use a small gas mass flow rate to process a large solids mass flow rate. This means that, for a given solids mass flow rate, one should choose the smallest possible gas mass flow rate that allows achieving a molar calcination conversion of 1. For the nominal operating condition $\dot{m}_s(0) = 0.01$ kg s^{-1}, it can be observed that the smallest possible gas mass flow rate is $\dot{m}_g(0) = 0.01$ kg s^{-1}, which also corresponds to the chosen operating condition. Furthermore, this condition for the mass flow rates corresponds to a gas/solids mass flow rate ratio of 1, which is the smallest one that allows achieving a molar calcination conversion of 1. For the smallest gas/solids mass flow rate ratio of 0.2, the calcination conversion decreases below 0.4.

3.3.3. Effect of the inlet mass fractions

Fig. 20 shows the molar calcination conversion for different values of inlet mass fractions of CO_2 and CaO around the nominal operating conditions. The best operating region for a higher molar calcination conversion corresponds to large inlet mass fractions of CaO and small inlet mass fractions of CO_2. Regarding the mass fraction of CO_2, this result is expected since a smaller fraction of CO_2 results in a smaller CO_2 concentration in the reactor, which leads to a larger reaction rate due to a larger difference between the equilibrium and local concentrations of CO_2. In fact, for larger mass fractions of CO_2, the reaction may not start at the beginning of the reactor because the local concentration of CO_2 may be larger than the equilibrium concentration until the bed temperature is sufficiently high to allow the reaction to start. On the other hand, for the mass fraction of CaO, although a smaller mass fraction of CaO results in a larger reaction rate due to a larger molar fraction of $CaCO_3$, the higher molar calcination conversion for larger mass fractions of CaO is caused by the fact that less $CaCO_3$ needs to be converted to CaO, which means that it is easier to achieve a higher molar calcination conversion. Hence, it can still be beneficial to use solid particles with a small mass fraction of CaO, because more $CaCO_3$ is converted to CaO. The results for different inlet mass fractions of CaO are relevant for the choice between a high-quality sorbent with a low deactivation and a consequent low mass fraction of CaO or a sorbent with a larger deactivation and a larger mass fraction of CaO.
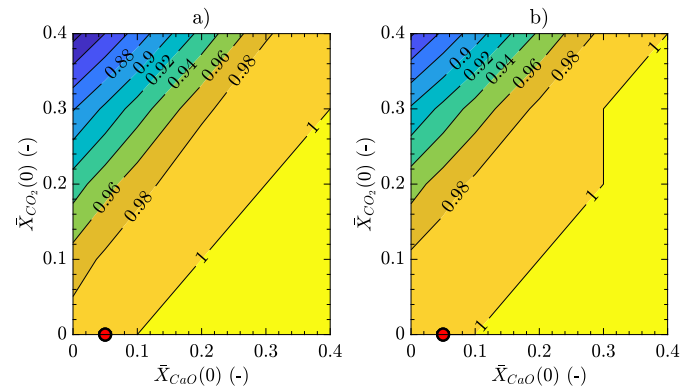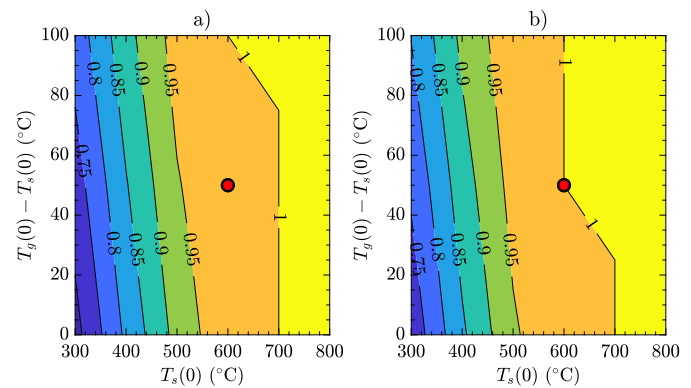
3.3.4. Effect of the inlet temperatures

Fig. 21 presents the molar calcination conversion for different values of inlet gas and solids temperatures around the nominal operating conditions. The best operating region for a high molar calcination conversion corresponds to large inlet temperatures for both gas and solids. In fact, as observed in Fig. 16, the reactor performance only depends on the inlet bed temperature after thermal equilibrium that is reached near the reactor inlet, given by the convex combination of the inlet gas and solids temperatures shown in (46), rather than the set of both inlet gas and solids temperatures. A lower inlet bed temperature implies that (i) more heat needs to be supplied from the wall to the bed to heat up the reactant such that the calcination reaction can take place, owing to a larger kinetic constant and CO_2 equilibrium concentration, which implies that the calcination reaction starts at a larger reactor height, and (ii) less heat is available to conduct the endothermic calcination reaction. Both effects cause a reduced molar calcination conversion. For the lowest inlet temperatures, the irradiance does not suffice to heat up the bed such that complete calcination can take place and the calcination conversion is decreased below 0.7. These results suggest the need to preheat the gas and solids before they are fed into the calciner and the use of a well-insulated storage system to decrease heat losses between the carbonator and the calciner.

For all the cases covered in this sensitivity analysis, the range of model parameters and operating conditions for which complete calcination is achieved is almost the same for both reactor heights of

4 m and 6 m. This further confirms that a reactor height between 4 m and 6 m is sufficient for a robust calciner operation with complete calcination.

4. Conclusions

This article presents a computational steady-state model of a solar calcination reactor for the Calcium-looping process for thermochemical energy storage in concentrating solar power systems. A reactor configuration that consists in an indirectly irradiated system was proposed. This reactor corresponds to an absorber tube that is exposed to concentrated solar radiation and plays the role of a riser of a continuous circulating fluidized bed where the reaction occurs. The fluidized bed is modeled in the axial dimension, while the reactor wall is modeled in both the axial and angular dimensions via the use of wall elements in the angular direction. The model allows imposing the concentrated solar irradiance on the wall and considering the effect of wall conduction in the angular direction. The model also considers the effect of fluid dynamics, reaction kinetics, and wall-bed heat transfer. In particular, a core-annulus heat transfer model is used in the lean zone of the reactor and a modified version of the Kunii–Levenspiel fluid dynamics model is considered. In contrast to previous work based on the Kunii–Levenspiel model, a novelty of the present work is that the variation in the mass flow rate of the species and in the density of the phases caused by the reaction is considered in the present model and is expected to provide more realistic results. The fluid dynamics and the heat transfer models were based on experimental results of CFBs which were not solar-driven calcination reactors, while the reaction kinetics model was based on experimental results of calcination reactors which were not solar-driven CFBs.

The results for the case of imposed concentrated solar irradiance with wall conduction in the angular direction show that it is possible to achieve a calcination conversion of 100% for a reactor height of less than 6 m. The results are similar when the wall conduction in the angular direction is excluded or the number of wall elements is reduced, allowing a more computationally efficient model. Moreover, a sensitivity analysis with respect to different operating conditions and model parameters was performed with constant concentrated solar irradiance. This analysis shows that the calcination conversion is sensitive to variations in the parameters of the fluid dynamics model and inlet conditions such as the gas and solids mass flow rates, mass fractions of CO_2 and CaO in the gas and solids, respectively, and gas and solids temperatures. In particular, the calcination conversion is significantly reduced for large inlet solids mass flow rates and low inlet temperatures. On the other hand, the calcination conversion is approximately constant for reactor heights between 4 m and 6 m regardless of the operating conditions and model parameters.

The proposed model is a useful and promising tool that (i) allows assessing the effect of design choices and aiming strategies for the solar radiation on several key variables such as the calcination conversion, the maximum wall temperature, and the bed temperature, which is required to avoid sintering of the sorbent, and (ii) considers the relevant physical phenomena while it remains relatively simple and efficient from a computational viewpoint. Hence, it allows obtaining quick results for the effect of different operating conditions and model parameters on the performance of a solar calcination reactor.

In future work, this model may be extended to the transient case, in which the inlet conditions and the concentrated solar irradiance vary with time, and the reactor model may be integrated with the solar field and the receiver cavity that encloses the reactor. Although radial variation in the reactor and space-dependent properties of the receiver cavity were considered out of the scope of this work to avoid making the model more complex and more computationally expensive, this would also be an interesting extension. Hence, this model is expected to allow testing different control strategies for the solar field and different reactor configurations such as a receiver cavity with several risers. This may facilitate scale-up and improve the robustness of the calcination reactor in the Calcium-looping process for thermochemical energy storage in concentrating solar power systems. This simulation study and the lack of corresponding experimental data for validation also reinforces the need for future experimental studies in high-temperature reaction systems for solar calcination. In any case, the model in the present paper may be useful to design experimental prototypes or pilot-scale reactors for solar-driven calcination of $CaCO_3$.

Declaration of competing interest

The authors declare that they have no known competing financial interests or personal relationships that could have appeared to influence the work reported in this paper.

Acknowledgments

Appendix A. Iterative procedure to compute the wall temperature

By defining the $n_{el} \times n_{el}$ matrix

$$\mathbf{S} = \begin{bmatrix} -2 & 1 & 0 & \cdots & 0 & 0 & 1 \\ 1 & -2 & 1 & \cdots & 0 & 0 & 0 \\ 0 & 1 & -2 & \cdots & 0 & 0 & 0 \\ \vdots & \vdots & \vdots & \ddots & \vdots & \vdots & \vdots \\ 0 & 0 & 0 & \cdots & -2 & 1 & 0 \\ 0 & 0 & 0 & \cdots & 1 & -2 & 1 \\ 1 & 0 & 0 & \cdots & 0 & 1 & -2 \end{bmatrix}, \tag{A.1}$$

and the n_{el}-dimensional vectors

$$\mathbf{T}_w(z) = \begin{bmatrix} T_{w,1}(z) & \cdots & T_{w,n_{el}}(z) \end{bmatrix}^{\mathrm{T}}, \tag{A.2}$$

$$\mathbf{h}_{w-b}(z) = \begin{bmatrix} h_{w-b,1}(z) & \cdots & h_{w-b,n_{el}}(z) \end{bmatrix}^{\mathrm{T}}, \tag{A.3}$$

$$\mathbf{H}_{irr}(z) = \begin{bmatrix} H_{irr,1}(z) & \cdots & H_{irr,n_{el}}(z) \end{bmatrix}^{\mathrm{T}}, \tag{A.4}$$

$$\mathbf{h}_{r,rad}(z) = \begin{bmatrix} h_{r,rad,1}(z) & \cdots & h_{r,rad,n_{el}}(z) \end{bmatrix}^{\mathrm{T}}, \tag{A.5}$$

the equality (77) can be expressed in terms of vectors as

$$\mathrm{diag}\left(\mathbf{h}_{w-b}(z)\right)\mathbf{T}_w(z) - T_b(z)\mathbf{h}_{w-b}(z)$$
$$= \mathbf{H}_{irr}(z) - \mathrm{diag}\left(\mathbf{h}_{r,rad}(z)\right)\mathbf{T}_w(z) + T_r\mathbf{h}_{r,rad}(z) + k_w d_w \left(\frac{\pi D}{n_{el}}\right)^{-2}\mathbf{S}\mathbf{T}_w(z), \tag{A.6}$$

which allows obtaining an explicit expression for $\mathbf{T}_w(z)$ at the next iteration as a function of the quantities computed at each iteration:

$$\mathbf{T}_w(z) = \left(\mathrm{diag}\left(\mathbf{h}_{w-b}(z)\right) + \mathrm{diag}\left(\mathbf{h}_{r,rad}(z)\right) - k_w d_w \left(\frac{\pi D}{n_{el}}\right)^{-2}\mathbf{S}\right)^{-1}$$
$$\left(\mathbf{H}_{irr}(z) + T_r\mathbf{h}_{r,rad}(z) + T_b(z)\mathbf{h}_{w-b}(z)\right). \tag{A.7}$$

References

Alvarez Rivero, M., Rodrigues, D., Pinheiro, C., Cardoso, J., Mendes, L., 2022. Solid–gas reactors driven by concentrated solar energy with potential application to calcium looping: A comparative review. Renew. Sustain. Energy Rev. 158, 112048.

Arias, B., Diego, M., Abanades, J., Lorenzo, M., Diaz, L., Martínez, D., Alvarez, J., Sánchez-Biezma, A., 2013. Demonstration of steady state CO2 capture in a 1.7MWth calcium looping pilot. Int. J. Greenh. Gas Control 18, 237–245.

Arias, B., Diego, M., Méndez, A., Alonso, M., Abanades, J., 2018. Calcium looping performance under extreme oxy-fuel combustion conditions in the calciner. Fuel 222, 711–717.

Basu, P., 2015. Circulating Fluidized Bed Boilers: Design, Operation and Maintenance. Springer International Publishing, Cham.

Bidwe, A.R., 2017. Hydrodynamic Studies of the Dual Fluidized Bed Reactor Systems for High Temperature Solid Looping Cycles (Ph.D. thesis). University of Stuttgart, Germany.

Błaszczuk, A., 2015. Effect of flue gas recirculation on heat transfer in a supercritical circulating fluidized bed combustor. Arch. Thermodyn. 36 (3), 61–83.

Brewster, M.Q., 1986. Effective absorptivity and emissivity of particulate media with application to a fluidized bed. J. Heat Transfer 108 (3), 710–713.

Charitos, A., Rodríguez, N., Hawthorne, C., Alonso, M., Zieba, M., Arias, B., Kopanakis, G., Scheffknecht, G., Abanades, J.C., 2011. Experimental validation of the calcium looping CO2 capture process with two circulating fluidized bed carbonator reactors. Ind. Eng. Chem. Res. 50 (16), 9685–9695.

Collado, F.J., 2016. New one-dimensional hydrodynamics of circulating fluidized bed risers. Granul. Matter 18 (4), 78.

Cormos, A.M., Simon, A., 2015. Assessment of CO2 capture by calcium looping (CaL) process in a flexible power plant operation scenario. Appl. Therm. Eng. 80, 319–327.

Craig, R.A., 2010. Investigating the Use of Concentrated Solar Energy to Thermally Decompose Limestone (Ph.D. thesis). University of Adelaide, Adelaide, Australia.

Dutta, A., Basu, P., 2005. An improved cluster-renewal model for the estimation of heat transfer coefficients on the furnace walls of commercial circulating fluidized bed boilers. J. Heat Transfer 126 (6), 1040–1043.

Erans, M., Manovic, V., Anthony, E.J., 2016. Calcium looping sorbents for CO2 capture. Appl. Energy 180, 722–742.

Fang, F., Li, Z.S., Cai, N.S., 2009. Experiment and modeling of CO2 capture from flue gases at high temperature in a fluidized bed reactor with Ca-based sorbents. Energy Fuels 23 (1), 207–216.

Fernandez, J.R., Turrado, S., Abanades, J.C., 2019. Calcination kinetics of cement raw meals under various CO2 concentrations. React. Chem. Eng. 4 (12), 2129–2140.

Grace, J.R., 1984. Hydrodynamics of gas fluidized beds. In: Basu, P. (Ed.), Fluidized Bed Boilers. Pergamon, pp. 13–30.

Hanak, D.P., Anthony, E.J., Manovic, V., 2015. A review of developments in pilot-plant testing and modelling of calcium looping process for CO2 capture from power generation systems. Energy Environ. Sci. 8, 2199–2249.

Harris, A., Davidson, J., Thorpe, R., 2002. The prediction of particle cluster properties in the near wall region of a vertical riser (200157). Powder Technol. 127 (2), 128–143.

Kuipers, J.A.M., Prins, W., Van Swaaij, W.P.M., 1992. Numerical calculation of wall-to-bed heat-transfer coefficients in gas-fluidized beds. AIChE J. 38 (7), 1079–1091.

Kunii, D., Levenspiel, O., 1991. High-velocity fluidization. In: Kunii, D., Levenspiel, O. (Eds.), Fluidization Engineering, second ed. Butterworth-Heinemann, Boston, pp. 193–210.

Kunii, D., Levenspiel, O., 2000. The K-L reactor model for circulating fluidized beds. Chem. Eng. Sci. 55 (20), 4563–4570.

Li, J., Tung, Y., Kwauk, M., 1988. Energy transport and regime transition in particle-fluid two-phase flow. In: Basu, P., Large, J.F. (Eds.), Circulating Fluidized Bed Technology. Pergamon, pp. 75–87.

Lisbona, P., Bailera, M., Hills, T., Sceats, M., Díez, L.I., Romeo, L.M., 2020. Energy consumption minimization for a solar lime calciner operating in a concentrated solar power plant for thermal energy storage. Renew. Energy 156, 1019–1027.

Lovegrove, K., Stein, W., 2012. Concentrating Solar Power Technology: Principles, Developments and Applications. Woodhead Publishing, Sawston, UK.

Martínez, I., Grasa, G., Murillo, R., Arias, B., Abanades, J., 2013. Modelling the continuous calcination of CaCO3 in a Ca-looping system. Chem. Eng. J. 215–216, 174–181.

Martínez, I., Grasa, G., Parkkinen, J., Tynjälä, T., Hyppänen, T., Murillo, R., Romano, M.C., 2016. Review and research needs of Ca-Looping systems modelling for post-combustion CO2 capture applications. Int. J. Greenh. Gas Control 50, 271–304.

Martínez, A., Lisbona, P., Lara, Y., Romeo, L.M., 2011. Carbonate looping cycle for CO2 capture: Hydrodynamic of complex CFB systems. Energy Procedia 4, 410–416.

Meier, A., Bonaldi, E., Cella, G.M., Lipinski, W., Wuillemin, D., Palumbo, R., 2004. Design and experimental investigation of a horizontal rotary reactor for the solar thermal production of lime. Energy 29 (5), 811–821.

Nikulshina, V., Gebald, C., Steinfeld, A., 2009. CO2 capture from atmospheric air via consecutive CaO-carbonation and CaCO3-calcination cycles in a fluidized-bed solar reactor. Chem. Eng. J. 146 (2), 244–248.

Nikulshina, V., Hirsch, D., Mazzotti, M., Steinfeld, A., 2006. CO2 capture from air and co-production of H2 via the Ca(OH)2–CaCO3 cycle using concentrated solar power–Thermodynamic analysis. Energy 31 (12), 1715–1725.

Ortiz, C., Romano, M.C., Valverde, J.M., Binotti, M., Chacartegui, R., 2018. Process integration of calcium-looping thermochemical energy storage system in concentrating solar power plants. Energy 155, 535–551.

Ortiz, C., Valverde, J.M., Chacartegui, R., Perez-Maqueda, L.A., Giménez, P., 2019. The calcium-looping (CaCO3/CaO) process for thermochemical energy storage in concentrating solar power plants. Renew. Sustain. Energy Rev. 113, 109252.

Pardo, P., Deydier, A., Anxionnaz-Minvielle, Z., Rougé, S., Cabassud, M., Cognet, P., 2014. A review on high temperature thermochemical heat energy storage. Renew. Sustain. Energy Rev. 32, 591–610.

Pinheiro, C.I.C., Fernandes, A., Freitas, C., Santos, E.T., Ribeiro, M.F., 2016. Waste marble powders as promising inexpensive natural CaO-based sorbents for post-combustion CO2 capture. Ind. Eng. Chem. Res. 55 (29), 7860–7872.

Rivero, M.A., Rodrigues, D., Pinheiro, C.I.C., Cardoso, J.P., Mendes, L.F., 2021. Modelling a calcium-looping fluidised bed calcination reactor with solar-driven heat flux. Chem. Eng. Trans. 88, 871–876.

Sánchez, R.A., Jakobsen, H.A., 2014. Modeling and simulation of circulating fluidized bed reactors applied to a carbonation/calcination loop. Particuology 15, 116–128.

Sans, J.L., Ballestrín, J., Guillot, E., Cros, A., Marzo, A., 2018. Comparisons of the Spectral Emissivity Measurements at High Temperatures of Stainless Steel AISI 310S. Technical Report.

Schöniger, F., Thonig, R., Resch, G., Lilliestam, J., 2021. Making the sun shine at night: comparing the cost of dispatchable concentrating solar power and photovoltaics with storage. Energy Sources B 16 (1), 55–74.

Sun, Z., Zhu, J., 2019. A consolidated flow regime map of upward gas fluidization. AIChE J. 65 (9), e16672.

Teixeira, P., Afonso, E., Pinheiro, C.I., 2022. Tailoring waste-derived materials for calcium-looping application in thermochemical energy storage systems. J. CO2 Util. 65, 102180.

Teixeira, P., Hipólito, J., Fernandes, A., Ribeiro, F., Pinheiro, C.I.C., 2019. Tailoring synthetic Sol–Gel CaO sorbents with high reactivity or high stability for Ca-looping CO2 capture. Ind. Eng. Chem. Res. 58 (19), 8484–8494.

Teixeira, P., Mohamed, I., Fernandes, A., Silva, J., Ribeiro, F., Pinheiro, C.I., 2020. Enhancement of sintering resistance of CaO-based sorbents using industrial waste resources for Ca-looping in the cement industry. Sep. Purif. Technol. 235, 116190.

Vignarooban, K., Xu, X., Arvay, A., Hsu, K., Kannan, A., 2015. Heat transfer fluids for concentrating solar power systems – A review. Appl. Energy 146, 383–396.

Xie, D., Bowen, B., Grace, J., Lim, C., 2003. Two-dimensional model of heat transfer in circulating fluidized beds. Part I: Model development and validation. Int. J. Heat Mass Transfer 46 (12), 2179–2191.

Xu, J., Lu, X., Zhang, W., Chen, J., Wang, Q., Chen, Y., Guo, Q., 2018. Effects of superficial gas velocity and static bed height on gas-solid flow characteristics in a 60-meter-high transparent CFB riser. Chem. Eng. J. 334, 545–557.

Ylätalo, J., 2013. Model Based Analysis of the Post-Combustion Calcium Looping Process for Carbon Dioxide Capture (Ph.D. thesis). Lappeenranta University of Technology, Finland.

Ylätalo, J., Parkkinen, J., Ritvanen, J., Tynjälä, T., Hyppänen, T., 2013. Modeling of the oxy-combustion calciner in the post-combustion calcium looping process. Fuel 113, 770–779.

Zeneli, M., Nikolopoulos, A., Nikolopoulos, N., Grammelis, P., Karellas, S., Kakaras, E., 2017. Simulation of the reacting flow within a pilot scale calciner by means of a three phase TFM model. Fuel Process. Technol. 162, 105–125.

Zhang, H., Benoit, H., Gauthier, D., Degrève, J., Baeyens, J., López, I.P., Hemati, M., Flamant, G., 2016. Particle circulation loops in solar energy capture and storage: Gas–solid flow and heat transfer considerations. Appl. Energy 161, 206–224.